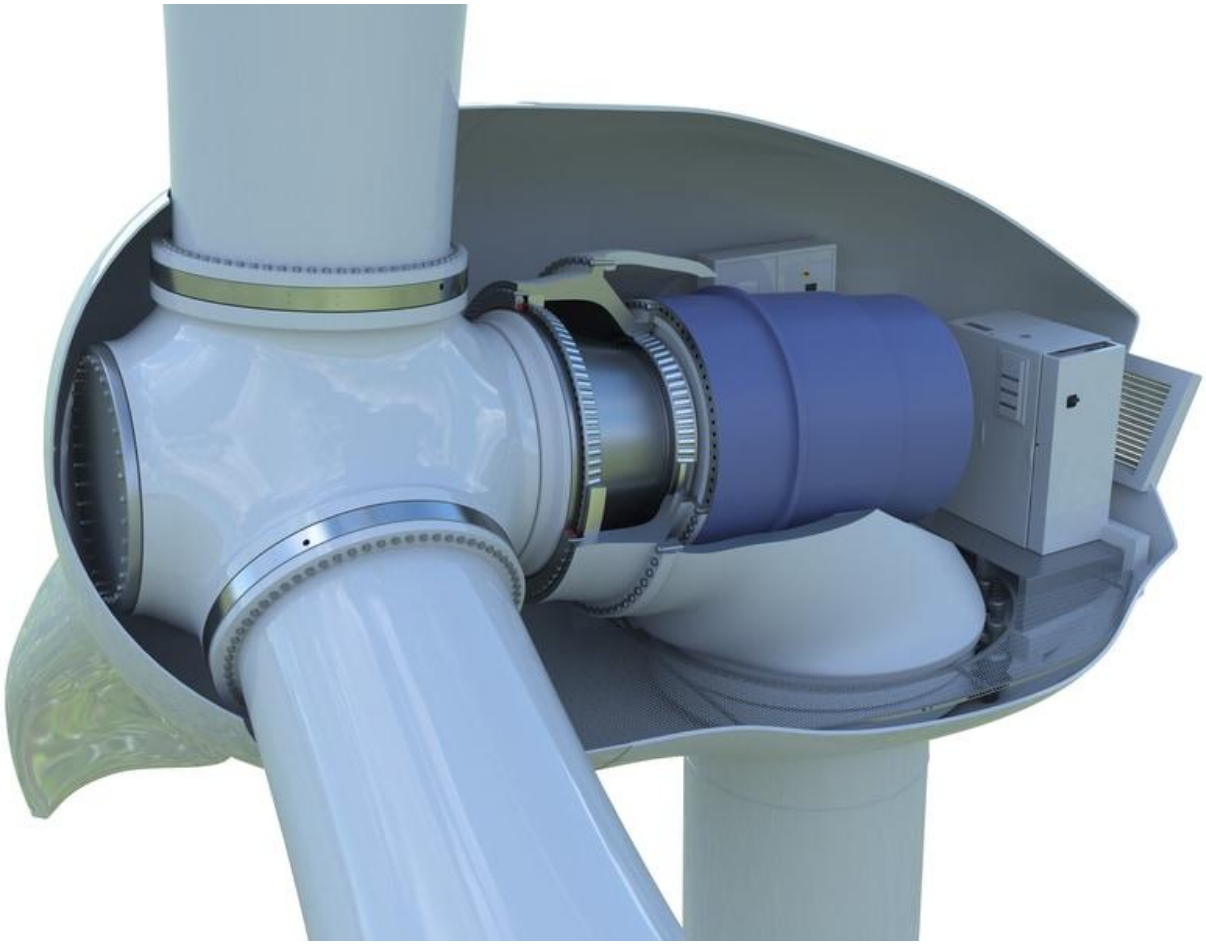

Parametric Study of Ring Creep in Wind Turbine Bearings

A FEA-Based Study of Structure-Induced Ring Creep in Wind Turbine Main Shaft Bearings

Master's thesis in Applied Mechanics

NIKHIL PRASAD KATTI

DEPARTMENT OF MECHANICS AND MARITIME SCIENCES

CHALMERS UNIVERSITY OF TECHNOLOGY
Gothenburg, Sweden 2026
www.chalmers.se

Master's Thesis in Applied Mechanics

Parametric Study of Ring Creep in Wind Turbine Bearings

A FEA-Based Study of Structure-Induced Ring Creep in Wind Turbine Main Shaft Bearings

NIKHIL PRASAD KATTI

CHALMERS
UNIVERSITY OF TECHNOLOGY

Department of Mechanics and Maritime Sciences
Chalmers University of Technology
Gothenburg, Sweden 2026

Parametric Study of Ring Creep in Wind Turbine Bearings
A FEA-Based Study of Structure-Induced Ring Creep in Wind Turbine Main Shaft Bearings
NIKHIL PRASAD KATTI

Supervisor: Denny Fritze, AECC Project Engineer, SKF
Examiner: Håkan Johansson, Professor, Chalmers University

Master's Thesis 2026
Department of Mechanics and Maritime Sciences
Chalmers University of Technology
SE-412 96 Gothenburg
Sweden
Telephone +46 31 772 1000

Cover: Model Wind-Turbine with visible internal bearing assembly. Image sourced from www.skf.com with permission.

Typeset in LaTeX
Gothenburg, Sweden 2026

Parametric Study of Ring Creep in Wind Turbine Bearings
A FEA-Based Study of Structure-Induced Ring Creep in Wind Turbine Main Shaft Bearings
NIKHIL PRASAD KATTI
Department of Mechanics and Maritime Sciences
Chalmers University of Technology

Abstract

Ring creep, the progressive circumferential migration of a bearing ring relative to its seat is a critical failure mode in large-scale wind turbine main shaft bearings, where aerodynamic bending moments produce non-uniform contact pressure distributions that classical interference fit calculations cannot reliably predict. This study presents an FEA-based case study developed at SKF AECC to quantify the influence of aerodynamic load components on structure-induced ring creep in a generic multi megawatt wind turbine arrangement. A multi-scale simulation framework couples system-level bearing load extraction in SKF SimPro with a non-linear, quasi-static transient finite element analysis in ANSYS, where contact load vectors are rotated in discrete angular increments across the inner ring raceway of a submodel comprising the main shaft and inner races of two large-size tapered roller bearings. A load component screening study identifies Tilt and Yaw moments as the dominant contributors to ring creep, motivating a systematic parametric study across the operational Tilt–Yaw loading space. The resulting response surfaces reveal a clear non-linear relationship between the applied bending moments and the ring creep behaviour, identifying critical load thresholds beyond which the interference fit transitions from stable micro-slip into irreversible macro-wandering. Integration of the simulation results with a recorded operational load history further shows that ring creep damage in this configuration is driven primarily by normal power produc tion loading rather than by extreme or rare load events, underscoring the practical importance of housing stiffness and interference fit specification at the drivetrain design stage. All quantitative results are specific to the structural stiffness of the generic housing and shaft geometry used in this study and should not be interpreted as generally applicable thresholds.

Keywords: ring creep, wind turbine bearings, structure-induced creep, interference fit, finite element analysis, tapered roller bearings, multi-scale modelling, parametric study, bending moments, fretting wear

Preface

This report presents the outcome of a master's thesis project carried out at SKF AECC (Advanced Engineering Competence Centre) in Gothenburg, in collaboration with the Department of Mechanics and Maritime Sciences at Chalmers University of Technology, during the spring of 2026. The work was conducted as part of the master's programme in Applied Mechanics and represents the culmination of two years of graduate study.

The thesis investigates structure-induced ring creep in large wind turbine main shaft bearings, a failure mode that has grown in practical relevance as turbine rotor diameters have continued to increase. The motivation for the study came from ongoing work within SKF AECC on improving the predictability of ring creep behaviour across the operational loading envelope of a wind turbine drivetrain. The simulation framework used here builds on an existing methodology within SKF, coupling system-level roller-load prediction analysis in SKF SimPro with a detailed non-linear finite element submodel in ANSYS, and extends it through a systematic parametric study across a representative range of aerodynamic load combinations.

The subject sits at the intersection of contact mechanics, structural finite element analysis, and wind turbine engineering, and required building familiarity with each of these areas over the course of the project. The work presented here reflects that learning process as much as it does the final results, and it is hoped that the framework and findings will serve as a useful reference for future ring creep assessments within SKF AECC.

Acknowledgements

I would like to thank my supervisor at SKF, Denny Fritze, for his guidance, technical insight, and patience throughout this project. His feedback consistently pushed the work in the right direction, and the discussions we had along the way shaped this thesis in more ways than one.

I am also grateful to my examiner, Professor Håkan Johansson at Chalmers, for his support and constructive input during the course of this work.

To my colleagues at SKF, thank you for the welcoming environment and for always being willing to answer questions, however basic they may have seemed.

Finally, to my family and friends, thank you for your encouragement and for tolerating the occasional weekend spent staring at ANSYS output.

Nikhil Prasad Katti, Gothenburg, June 2026

List of Acronyms

Below is the list of acronyms that have been used throughout this thesis listed in alphabetical order:

AECC	Advanced Engineering Competence Centre
APDL	ANSYS Parametric Design Language
CAD	Computer-Aided Design
CMS	Component Mode Synthesis
CPU	Central Processing Unit
DOF	Degree of Freedom
FEA	Finite Element Analysis
FEM	Finite Element Method
FKN	Contact Normal Stiffness Factor (ANSYS)
IR	Inner Ring
KDE	Kernel Density Estimate
RAM	Random Access Memory
SKF	Svenska Kullager-Fabriken
SSD	Solid State Drive
TRB	Tapered Roller Bearing

Nomenclature

Below is the nomenclature of symbols and variables that have been used throughout this thesis.

C_{acc}	Accumulated slip per evaluation cycle	[μm/rev]
C_{eff}	Effective creep per evaluation cycle	[μm/rev]
d	Nominal fit diameter	[m]
d_i	Inner diameter of the shaft	[m]
d_o	Outer diameter of the hub	[m]
E_i, E_o	Young's modulus of inner / outer component	[Pa]
f	Maximum transmissible tangential force per unit length	[N/m]
h	Kernel bandwidth	–
K	Gaussian kernel function	–
L	Axial fit length	[m]
M_x	Tilt moment	[kNm]
M_y	Roll moment	[kNm]
M_z	Yaw moment	[kNm]
N	Number of recorded operating points / load steps	–
p_0	Nominal interference fit contact pressure	[Pa]
p_{local}	Local contact pressure at ring seat	[Pa]
s	Relative slip distance	[μm]
s_{ref}	Local creep as a function of load angle φ	[μm]
s_{off}	Initial offset creep prior to load rotation	[μm]
t_i	Time share at operating point i	[min]
w_i	Creep-weighted time share at operating point i	–
W_{slip}	Frictional work dissipated at ring seat interface	[J]
δ	Diametral interference	[μm]
Δs	Oscillatory slip delta (peak-to-peak amplitude)	[μm]
μ	Coefficient of friction	–
ν_i, ν_o	Poisson's ratio of inner / outer component	–
τ	Local shear stress at ring seat interface	[Pa]
τ_{local}	Local shear stress from regularised Coulomb model	[Pa]
φ	Angular position of the rotating load vector	[°]
$\hat{f}$	Unweighted kernel density estimate	–
$\hat{f}_w$	Creep-weighted kernel density estimate	–
$\hat{f}_{\text{creep}}$	Normalised annual creep map	[mm/yr]

Subscripts

i	Inner component (shaft)
o	Outer component (hub / ring)
end, start	End and start of one evaluation cycle
acc	Accumulated (total absolute slip)
eff	Effective (net slip per revolution)
ref	Reference node for local creep evaluation
tot	Total (global creep integrated over all nodes)

Contents

List of Figures

List of Tables

1

Introduction

1.1 Background

Rolling bearings are among the most mechanically loaded components in a wind turbine drivetrain, and their reliability is a primary determinant of the availability and operational cost of the entire system [5, 3]. One failure mode that has received growing attention as turbine sizes have increased is ring creep. In the bearing literature, ring creep is broadly defined as the slow, progressive circumferential migration of a bearing ring relative to its mating seat surface, arising from the repeated elastic deformation of the ring under a rotating or oscillating contact load [13, 14]. At SKF, the definition is broader: any relative circumferential motion between the ring and its seat, including purely oscillatory back-and-forth movement without net drift is classified as ring creep, since both forms of micro-motion produces surface damage and degrades the integrity of the interference fit over time.

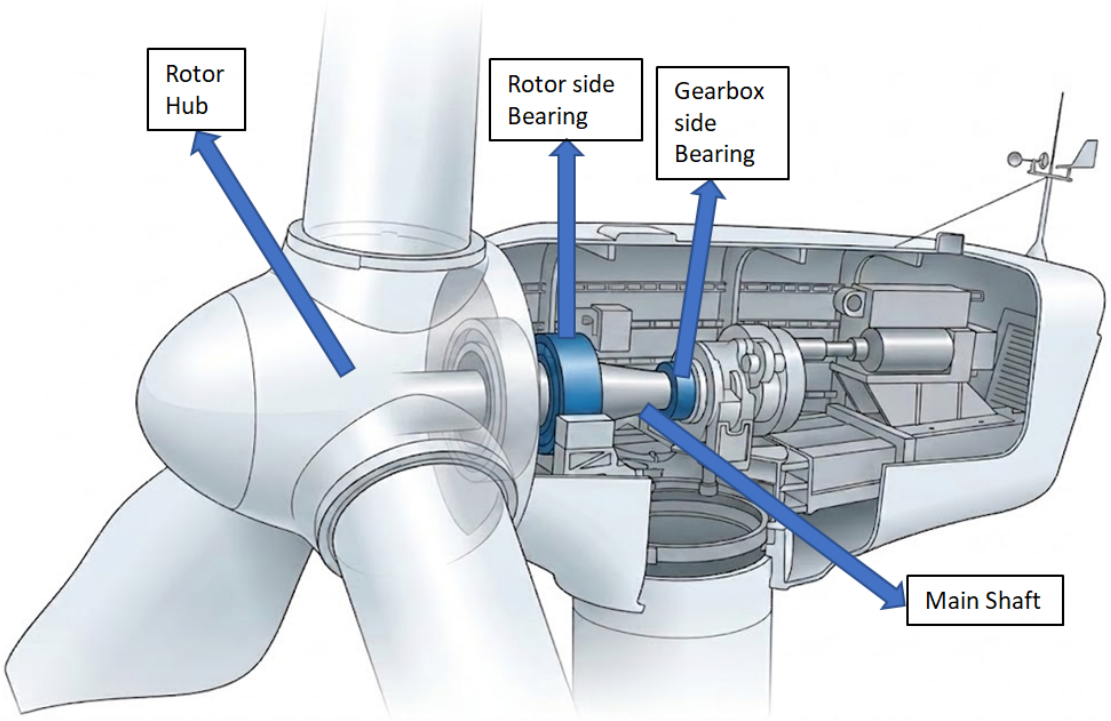

Figure 1.1: Generic Image of Wind Turbine Bearing Assembly

1.1.1 Ring Creep as a System-Level Failure Mode

Historically, ring creep was treated as a localised bearing problem, attributed primarily to an undersized interference fit or excessive radial loading. Research over the past decade has fundamentally changed this understanding. In large wind turbine main shaft bearings, ring creep is now recognised as a system-level structural failure mode, driven not by fit specification alone but by the elastic deformation of the surrounding drivetrain components under operational loads [5, 3]. This specific mechanism is referred to as structure-induced creep, and it is the central subject of this study. SKF further distinguishes two additional creep mechanisms: drag-induced creep, caused by rolling friction of the rolling elements on the raceway, and roller-induced creep, arising from the travelling elastic wave generated by individual roller passages. In wind turbine main bearings, structure-induced creep is the dominant mechanism because the housing and shaft are large, flexible structures, and the number of rollers in large-size bearings is relatively high whose elastic deformation under bending moments is of comparable magnitude to the initial interference pressure at the ring seat [2, 7].

1.1.2 The Scaling Challenge in Wind Turbine Bearings

The rapid growth of wind turbine rotor diameters towards and beyond three metres has introduced a fundamental limitation in classical bearing design practice. Interference fit calculations based on standards such as DIN 7190-1 [6] assume axisymmetric loading and a nominally rigid housing — an assumption that is adequate for small and medium sized industrial bearings but breaks down at the scale of modern multi-megawatt drivetrains [5, 2]. As rotor diameter increases, the bending moments acting on the main shaft grow with the square of the rotor radius, while the interference pressure scales only linearly with the diametral interference [5, 3]. The result is that large diameter bearings are inherently more susceptible to structure-induced ring creep than smaller bearings operating under equivalent specific load levels [5, 2]. Traditional analytical models are therefore no longer sufficient, and a simulation-based approach that explicitly represents the structural flexibility of the drivetrain is required to predict ring creep behaviour reliably.

1.1.3 The Role of Aerodynamic Bending Moments

A defining characteristic of the wind turbine operational environment is the presence of large, multi-axial bending moments at the rotor hub. The Tilt moment, which is dominated by the weight of the rotor itself with a superimposed aerodynamic oscillation, and the Yaw moment, driven by wind direction changes and turbulence, are the primary aerodynamic load components acting on the main shaft. These moments produce a non-uniform distribution of contact pressure around the bearing seat circumference, locally reducing the normal force at the ring-seat interface below the threshold required to sustain static friction [1, 3]. Where this threshold is exceeded, a slip zone forms and micro-motion initiates. The interaction between the rotating load induced slip zone and the spatially fixed structural deformation of the housing is what drives structure-induced ring creep in this application, and

understanding this interaction across the operational Tilt and Yaw loading space is the central objective of this study.

1.1.4 The Need for Numerical Simulation

Full-scale physical testing of metre-diameter main shaft bearings is prohibitively expensive and logistically complex, making high-fidelity finite element simulation the primary engineering tool for ring creep assessment in industrial practice. The simulation approach used in this study builds on an existing methodology developed within SKF, which combines system-level bearing load extraction using dynamic substructuring in SKF SimPro with a local non-linear finite element submodel in ANSYS. A key practical advantage of this approach is that the SimPro drivetrain models required for ring creep analysis are the same models already maintained for bearing life prediction in every wind turbine project, meaning that no additional global modelling effort is needed. The local ANSYS submodel then resolves the micrometre-scale slip accumulation at the ring-seat interface using a quasi-static load rotation approach, which is computationally efficient and numerically stable for the slow rotational speeds characteristic of wind turbine main shafts [3, 9].

1.2 Purpose

This study is carried out as part of ongoing work at SKF AECC on structure-induced ring creep in wind turbine main shaft bearings. The purpose is to conduct an exemplary case study that visualises and quantifies the influence of aerodynamic load components on ring creep behaviour across the operational loading envelope. The findings are intended to enable prediction of ring creep risk in operation in a manner analogous to established bearing life prediction methodology, providing a practical design tool for evaluating interference fit integrity under realistic wind turbine loading conditions.

1.3 Objectives

The specific objectives of this study are as follows:

1. To identify which aerodynamic load components produce significant variation in the bearing roller load distribution and therefore contribute meaningfully to ring creep behaviour.
2. To map the effective creep rate and accumulated slip across a systematic range of loads and to identify the critical load threshold beyond which stable micro-slip transitions to irreversible macro-wandering.
3. To integrate the simulation results with a recorded operational load history to estimate annual creep accumulation and identify which regions of the operational envelope dominate the long-term damage accumulation.

1.4 Scope and Limitations

The following points define the scope of this study and the deliberate simplifications adopted in the simulation approach:

- The finite element analysis is quasi-static in nature. This is a fit-for-purpose modelling choice: the high-frequency dynamic and thermal transients present in real wind turbine operation are highly uncertain and their input parameters are largely unknown, making their inclusion in the model neither practical nor meaningful for the purposes of this study.
- A uniform and static coefficient of friction is assumed throughout the contact domain. This represents an unbiased, as-assembled contact condition. The evolution of friction during service is not modelled and is not within the scope of this study.
- The global drivetrain loads are applied as static load cases in SKF SimPro rather than as a full dynamic load time series. This is a deliberate simplification that enables a systematic parametric study to be conducted efficiently within the computational resources and time.
- Wear accumulation at the ring-seat interface is not modelled. The study predicts creep rates for a nominally unworn contact condition.
- No design modifications or geometric recommendations are proposed within the scope of this work. The study is limited to characterising ring creep behaviour as a function of the applied load envelope and results for critical loads for creep are specific to the Assembly design used in this study.

2

Theory

2.1 Ring Creep in Rolling Bearings

2.1.1 Definition and SKF Classification

In the bearing literature, ring creep is broadly defined as the slow, progressive circumferential migration of a bearing ring relative to its mating seat surface, arising from the repeated elastic deformation of the ring under a rotating or oscillating contact load [13, 14]. At SKF, this definition is extended further. Any relative circumferential motion between the ring and its seat, including purely oscillatory back and forth movement without a net angular shift, is classified as ring creep, since both forms of micro motion produce surface damage and degrade the integrity of the interference fit over time.

Within this broader classification, SKF distinguishes three creep mechanisms according to their physical origin. Drag induced creep is caused by the rolling friction of the rolling elements on the raceway and does not necessarily require any clearance at the fit. Structure induced creep arises from the elastic deformation of the surrounding structure, such as the housing and shaft. Roller-induced creep results from a travelling elastic wave generated locally at each roller passage, in a manner analogous to the travelling wave mechanism described for plain bearings by Niwa [15], but acting at the much smaller length scale of an individual roller contact. The term "travelling wave", however, is not limited to roller-induced creep. In structure-induced creep, it also creates a travelling wave, but on a bigger scale driven by the loaded zone. Structure-induced creep is the mechanism investigated in this study.

2.1.2 Consequences of Ring Creep

Regardless of the underlying mechanism, repeated micro motion at the ring seat interface dissipates mechanical energy through interfacial friction. This drives fretting wear, characterised by the generation of fine oxidised debris at the contact interface, and contributes to the contamination of the surrounding lubricant by wear particles [16, 14]. Over time, this surface degradation progressively alters the local static coefficient of friction: fine oxide debris can initially reduce friction by acting as a solid lubricant, but continued surface damage may increase it by roughening and gouging the mating surfaces, lowering the effective threshold load at which further micro-slip initiates and creating a self-reinforcing process that can ultimately compromise the integrity of the interference [12].

2.2 Interference Fit Theory

2.2.1 Contact Pressure and Frictional Capacity

An interference fit is formed when the shaft's outer diameter exceeds the bore diameter of the mating component by a controlled amount δ, known as the diametral interference. Here, the bearings are usually press-fit onto the main shaft. Upon assembly, the resulting elastic deformation generates a nominally uniform radial contact pressure p_0 at the interface, which provides the frictional resistance required to prevent relative motion between the two components. For two concentric thick-walled cylinders in contact, the interface pressure is given by the Lame equation [6]:

$$p_0 = \frac{\delta}{d} \cdot \frac{1}{\frac{1}{E_i}\left(\frac{d_o^2 + d^2}{d_o^2 - d^2} + \nu_i\right) + \frac{1}{E_o}\left(\frac{d^2 + d_i^2}{d^2 - d_i^2} - \nu_o\right)}, \tag{2.1}$$

where d is the nominal fit diameter, d_o and d_i are the outer and inner diameters of the hub and shaft respectively, E_i and E_o are the elastic moduli, and ν_i and ν_o are the Poisson ratios of the respective components. The maximum transmissible tangential force per unit length is $f = \mu \cdot p_0 \cdot \pi \cdot d \cdot L$, where μ is the coefficient of friction and L is the axial fit length. This expression provides the analytical upper bound on the frictional load capacity that is used to motivate the interference values selected in Section 3.2.3.1 [6]. Tolerance specifications for bearing interference fits are governed by DIN 7190-1 [6], which prescribes minimum interference values to prevent slip under all design load conditions.

2.2.2 Pressure Degradation Under Bending

The Lame solution assumes axisymmetric loading and a perfectly cylindrical contact. In the presence of large bending moments, however, the shaft undergoes flexural deformation that introduces a non-uniform circumferential distribution of contact pressure at the fit interface. On the compression side, the local pressure is enhanced, while on the tension side it is reduced and may locally approach zero [5, 7]. Wherever the local contact pressure falls below the threshold required to sustain static friction, a slip zone forms. The circumferential extent of this slip zone and the magnitude of the local pressure deficit together determine the slip increment per load cycle and, by extension, the ring creep rate [8, 14].

This sensitivity is strongly amplified in large diameter bearings. The bending moment required to produce a given pressure deficit grows with the square of the rotor radius, while the interference pressure scales only linearly with the diametral interference. Large size tapered roller bearings of the type used in multi megawatt wind turbines are therefore inherently more susceptible to structure-induced ring creep than smaller bearings operating under equivalent specific load levels [12, 2].

2.3 Contact Mechanics at the Ring Seat Interface

2.3.1 Regularised Coulomb Friction Model

The frictional behaviour at the ring seat interface is governed by a regularised form of the Coulomb friction law, in which a small amount of elastic slip is permitted within the contact algorithm before gross sliding occurs. This differs from the classical Coulomb criterion, which defines a sharp transition between sticking and sliding at the point where the local shear stress equals the product of the friction coefficient and the local normal contact pressure. In the regularised formulation, the local shear stress τ_{local} increases approximately linearly with elastic slip up to the frictional limit $\mu \cdot p_{\text{local}}$, after which slip becomes irreversible. This regularisation improves the numerical stability and convergence of the non-linear contact solution while preserving the underlying frictional limit that governs the onset of macro level sliding [4].

2.3.2 Stick Slip Behaviour and Surface Degradation

The mechanics of the ring seat interface under cyclic tangential loading are characterised by two regimes. In the micro-slip regime, the applied bending moment is sufficient to locally reduce the contact pressure below the frictional threshold over a limited arc of the circumference. Within this arc, the interface undergoes small, reversible elastic slip that partially reverses each half-cycle as the load rotates. Because the positive and negative slip increments are of similar magnitude, they largely cancel over one full load rotation, resulting in negligible net circumferential migration despite significant oscillatory motion [16, 12]. As the severity of the applied bending moment increases, the slip arc expands progressively; once a critical threshold is exceeded, the asymmetry between the forward and return slip increments becomes sufficient to sustain a positive net displacement per cycle, and the ring enters the macro-wandering regime, characterised by continuous net circumferential drift [2, 12, 16].
The frictional work performed at the interface during this process is defined as:

$$W_{\text{slip}} = \tau \cdot s, \tag{2.2}$$

where τ is the local shear stress and s is the relative slip distance. This quantity represents the total mechanical energy dissipated through interfacial friction per unit area and is a physically complete metric for fretting damage severity [16]. In the present study, the accumulated slip (Section 4.3.2) is used as a computationally convenient surrogate that is proportional to W_{slip} in zones of active contact, and correlates directly with the total sliding path length at the interface.

2.4 Creep Metrics

The quantitative characterisation of ring creep from the finite element nodal output requires several related but distinct metrics, defined here in order of increasing scale.

2.4.1 Local and Global Creep

Local creep describes the relative tangential displacement between the inner ring bore and the shaft outer diameter at a single point on the circumference, evaluated as a continuous function of the angular position ϕ of the rotating load vector, where ϕ increases in the direction of load rotation. The sign convention adopted throughout this study follows the post-processing framework of [3, 2], a positive local displacement corresponds to ring migration in the same direction as the applied load rotation; a negative displacement corresponds to migration in the opposing direction. This raw displacement, denoted $s_{\text{ref}}(\phi)$, includes an initial offset arising from the assembly of the interference fit and the application of the static gravitational and structural loads prior to the start of the rotating load sequence. This initial offset, s_{off}, is subtracted from the raw output so that all subsequent creep metrics are referenced to the loaded-but-unrotated state of the assembly:

$$s(\phi) = s_{\text{ref}}(\phi) - s_{\text{off}}. \tag{2.3}$$

Global creep describes the circumferential average of the local creep over all possible reference node positions on the ring. At any angular position ϕ of the rotating load vector, the global creep $\bar{s}(\phi)$ is defined as:

$$\bar{s}(\phi) = \frac{1}{2\pi} \int_0^{2\pi} s_\theta(\phi)\, \mathrm{d}\theta, \tag{2.4}$$

where $s_\theta(\phi)$ is the local creep at the node located at circumferential angle θ, evaluated at load vector position ϕ. Because the local creep curves at different circumferential positions share the same waveform shape but are mutually phase-shifted by their angular separation θ, the oscillatory components cancel under the average and $\bar{s}(\phi)$ reduces to a smoothly linear function of ϕ. The slope of this linear trend is equal to the effective creep C_{eff} per full load rotation, as defined in Section 2.4.2.

2.4.2 Effective Creep

Effective creep represents the net circumferential migration of the ring accumulated over one complete rotation of the load vector. For a continuous loading case, it is defined as the difference between the local creep at the end and at the start of one full evaluation cycle:

$$C_{\text{eff}} = s_{\text{ref}}(\phi_{\text{end}}) - s_{\text{ref}}(\phi_{\text{start}}). \tag{2.5}$$

A positive value of C_{eff} indicates net migration in the same direction as the applied load rotation, while a negative value corresponds to migration in the opposing direction, following the sign convention defined in Section 2.4.1 [2, 3].

2.4.3 Accumulated Slip

Accumulated slip integrates the absolute magnitude of all incremental local creep values over one complete evaluation cycle, irrespective of their direction:

$$C_{\text{acc}} = \sum_{i=1}^{N-1} \left| s_{\text{ref}}(\phi_{i+1}) - s_{\text{ref}}(\phi_i) \right| . \tag{2.6}$$

where ϕ_i and ϕ_{i+1} denote consecutive angular positions of the load vector separated by the angular increment $\Delta\phi = \phi_{i+1} - \phi_i$ used in the quasi-static load rotation (see Section 2.5.1). Unlike effective creep, which captures only the net displacement, accumulated slip captures the total sliding path length traversed at the interface during one cycle. It is therefore proportional to the total frictional work dissipated in zones of active contact at the bearing seat per revolution, as expressed through Equation 2.2, and serves as a primary indicator of fretting wear risk even in load cases where the net effective creep is low [12, 16].

2.4.4 Oscillatory Slip Delta

The oscillatory slip delta measures the peak to peak amplitude of the local creep within a single evaluation cycle:

$$\Delta s = \max_{\phi} \, s_{\text{ref}}(\phi) - \min_{\phi} \, s_{\text{ref}}(\phi). \tag{2.7}$$

This metric quantifies the magnitude of the purely oscillatory, reversible component of the ring motion and is primarily relevant for assessing abrasive wear potential at the ring seat, independently of whether net migration is occurring [12, 16].

2.5 Numerical Simulation of Ring Creep

2.5.1 Multi-Scale Modelling

Simulating ring creep requires bridging global drivetrain dynamics and localised interface tribology across length scales that differ by several orders of magnitude. A monolithic finite element model resolving all relevant physics simultaneously is computationally intractable. The established approach instead employs a hierarchical submodelling strategy: global system level contact loads are first obtained from a reduced order drivetrain model using dynamic substructuring, and these are subsequently applied as boundary conditions to a high fidelity local finite element model of the bearing seat region [3, 9, 1]. This approach has been validated against full scale test rig measurements by Billenstein et al. [2, 1] and applied to wind turbine main shaft bearings by Grosse and Kyling [3].

2.5.2 Quasi-Static Load Rotation

Direct transient simulation of shaft rotation over millions of revolutions is computationally intractable. Instead, a quasi static load rotation approach is employed, in which the contact load vector is stepped through discrete angular positions around the bearing circumference rather than rotating the shaft itself [2, 8]. Reversing the direction of rotation in this manner produces an equivalent relative motion at the contact interface while avoiding the numerical instabilities associated with large

rigid body rotations in a non-linear finite element model. At each angular step, a non-linear static contact analysis is solved to obtain the instantaneous interfacial traction and displacement fields. The incremental tangential displacement extracted at each step provides the local creep contribution for that load increment, which is accumulated over a full evaluation cycle to yield the creep metrics defined in Section 2.4.

This approach is well suited to wind turbine main shaft bearings, where rotational speeds are low and the dominant aerodynamic bending moments vary slowly relative to the timescale of the contact mechanics at the ring seat. The high frequency dynamic and thermal transients present in real operation are therefore not expected to significantly influence the slip accumulation mechanism, supporting the use of a quasi static rather than fully transient dynamic formulation [3, 2].

2.5.3 Mapping Creep Across the Operational Load Envelope

The parametric finite element study yields effective creep and accumulated slip values at a discrete set of Load combinations identified through the screening study described in Section 3.4.3. To translate these discrete results into a continuous response surface over the full loading domain, an Ordinary Kriging interpolation with a Gaussian variogram model is applied, refined onto a dense grid using a bivariate spline. Once all parametric design points have been post processed, this Kriging based response surface converges to a result consistent with a direct cubic spline interpolation of the same data, since the underlying dataset is by that stage fully populated and no longer benefits from the spatial estimation properties of Kriging. Kriging was retained as the interpolation method throughout the study because it allowed response surface estimates to be generated and inspected at intermediate stages of the parametric study, providing early visibility of emerging trends in the loading space.

2.5.4 Linking Simulation Results to Operational Load Data

A continuous creep response surface alone does not indicate how much damage a turbine will accumulate in service, since this depends equally on how frequently each load combination is encountered during operation. To combine the response surface with a recorded operational load history, the unweighted and weighted Gaussian kernel density estimates (KDE) of the operational load history are computed over the Tilt and Yaw coordinate space (M_z, M_x).

It should be noted that an equivalent integration could be performed using a discretised histogram over the same coordinate space, with the same final outcome. The KDE approach is adopted here because it produces a smooth, continuously differentiable density estimate that overlays naturally with the Kriging response surface, simplifying visual inspection of the load distribution relative to the creep map. The unweighted and creep-weighted Gaussian kernel density estimates are computed as:

$$\hat{f}(M_z, M_x) = \frac{1}{Nh^2} \sum_{i=1}^{N} K\left(\frac{M_z - M_{z,i}}{h}, \frac{M_x - M_{x,i}}{h}\right), \tag{2.8}$$

$$\hat{f}_w(M_z, M_x) = \frac{1}{\sum_i w_i \, h^2} \sum_{i=1}^{N} w_i \, K\left(\frac{M_z - M_{z,i}}{h}, \frac{M_x - M_{x,i}}{h}\right), \tag{2.9}$$

where K is the Gaussian kernel, h is the kernel bandwidth, N is the number of recorded operating points, and w_i is the weight assigned to point i. For the annual creep mapping, the weight is computed from the total creep at load step i, $C_{\mathrm{tot},i}$, and the corresponding time share t_i, converted to a creep rate in millimetres per year:

$$w_i = |C_{\mathrm{tot},i}| \cdot \frac{365 \times 24 \times 60}{1000 \times 100}. \tag{2.10}$$

The weighted density is then divided by the unweighted density to obtain the normalised annual creep map:

$$\hat{f}_{\mathrm{creep}}(M_z, M_x) = \frac{\hat{f}_w(M_z, M_x)}{\hat{f}(M_z, M_x)}. \tag{2.11}$$

This normalisation step corrects for the fact that some regions of the loading space are sampled more densely than others purely due to how frequently the turbine operates there, so that the resulting map reflects the creep rate intrinsic to each load region rather than simply how often that region occurs in the dataset. This approach allows the most damaging regions of the operational loading envelope to be identified, in a manner analogous to established bearing life prediction methodology.

3
Methods

3.1 Workflow Overview

The methodology employed in this study follows a multi scale numerical framework designed to bridge the gap between global wind turbine dynamics and localised contact mechanics at the bearing seat. A hybrid system to submodel approach is used, transitioning from global drivetrain load extraction in SKF SimPro to a non linear finite element submodel in ANSYS, as illustrated in Figure 3.1. The SimPro analysis is static and provides the roller contact loads for the bearing arrangement, while the ANSYS analysis is quasi-static and resolves the resulting interfacial slip at the ring seat under a rotating load. The justification for each of these modelling choices is given in Chapter 2 and is revisited where relevant in the sections below. Based on that, the following figure shows the workflow for our study.

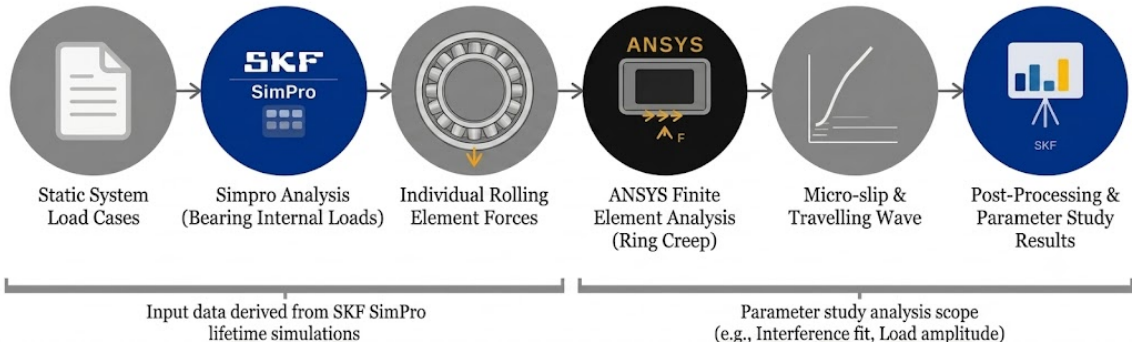

Figure 3.1: Workflow methodology followed for this study

3.2 Design

The chosen example is a generic model based on typical wind turbines in the medium-power class. It contains a preloaded back-to-back TRB-TRB-arrangement. The models are designed 1:1 with realistic dimensions in Ansys SpaceClaim 2024 R2.

3.2.1 Main Bearing Assembly

The main body of our wind turbine consists of a Housing which is fixed, and a main shaft which is rotating. This setup is connected using two bearings whose outer rings

are fit into the housing and the inner rings are on the shaft. The generic model is a highly weight-optimised design used to amplify bending-induced ovalization at the bearing seat, a design choice that maximises the sensitivity of the model to structure-induced creep and has realistic dimensions.

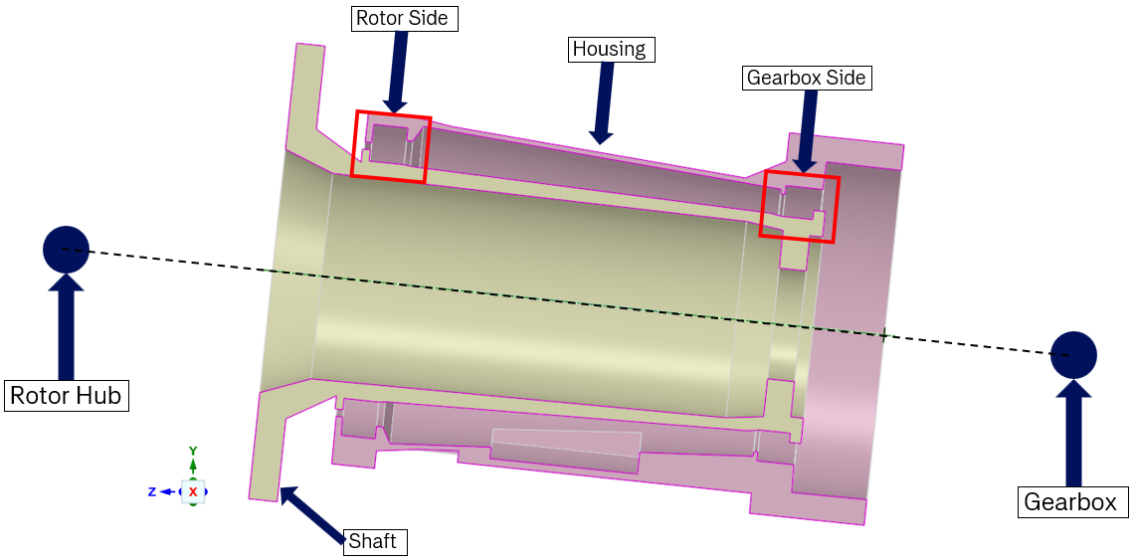

Figure 3.2: Cross-Section view of the Generic Model of the wind turbine

3.2.2 Material Properties

Table 3.1 summarises the mechanical material properties used for all components of the model, expressed in commonly used engineering units. The shaft, housing and bearings are modelled as flexible bodies using standard cast iron, a material widely used for large cast drivetrain components due to its favourable casting properties and adequate stiffness for structures of this scale. In SKF SimPro, the bearing rings are represented via a bonded contact formulation at the ring-seat interface, which transmits the elastic deformation of the surrounding housing and shaft directly to the roller contact load distribution without explicitly resolving the ring flexibility. This modelling approach is justified because the elastic deformation of the bearing rings themselves is several orders of magnitude smaller than the deformation of the surrounding shaft and housing under the applied bending moments, and therefore does not contribute meaningfully to the structural ovalization of the bearing seat that drives ring creep [5, 3].

Component	Young's Modulus (GPa)	Poisson's Ratio	Density (kg/m^3)
Shaft and Housing	170	0.28	7200
Bearings	206	0.30	7850

Table 3.1: Material properties of the shaft, housing, and bearings

3.2.3 Bearings

For the bearings, we use two large-size taper roller bearings from SKF, which are located at the Rotor Side (B1) and Gearbox Side (B2) of the wind turbines connecting the housing and the main shaft. The current focus is to investigate only the rotor side bearing. Although the gearbox side bearing must be included because we need the preloaded equilibrium. The following table shows the dimensions of these bearings.

Bearing	ID (mm)	OD (mm)	Width (mm)	Bearing type
Rotor Side (B1)	1500	2000	250	TRB
Gearbox Side (B2)	1400	1800	200	TRB

Table 3.2: Bearings specifications

3.2.3.1 Interference Fit

Both bearings are assembled with interference fits selected in accordance with DIN 7190 [6]: 800 μm diametral interference for the rotor side bearing and 720 μm for the gearbox side bearing. These values represent the minimum interference required at the respective fit diameters to prevent slip under the design load conditions, and provide the nominal contact pressure from which the sensitivity to bending-induced pressure degradation is evaluated.

3.3 Loads and Boundary Conditions

This study is carried out in the *SKF SimPro Expert* to get the contact loads in the bearings from the practical operational loads generally used for structural calculation on a wind turbine. The load data are chosen as a representative example to illustrate the workflows that are characteristic of the multi-megawatt wind turbine class. The following are the locations in the SimPro model where the loads are applied and the vectors in Figure 3.4 show the direction of the net resultant at that location.

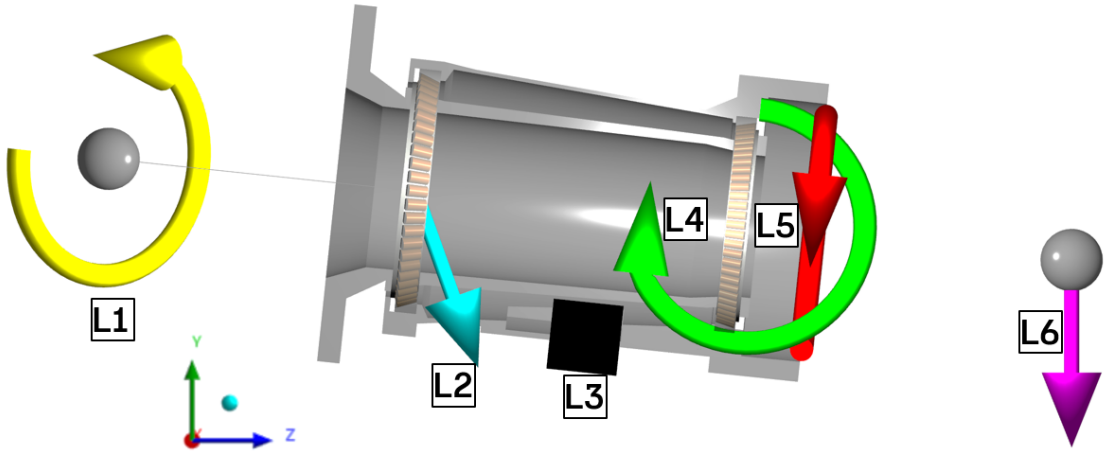

Figure 3.3: Resultant Locations of Loads and Boundary

The following are the details of the Load information

- The full model is subject to a gravity load of 9.81 m/s^2.
- **L1** is the resultant bending moment combining Tilt, Roll, and Yaw moments, denoted M_x, M_y, and M_z as given in Table 3.3. This moment is applied at the hub center, located approximately 2500 mm from the rotor side bearing.
- **L2** is the resultant force combining Lateral, Thrust, and Vertical components, denoted F_x, F_y, and F_z as given in Table 3.3. This force is applied at the center of the rotor side bearing.
- **L3** represents the ground condition, where the rigid body motion is prevented at the feet of the housing, fixing it for all DOFs.
- **L4** is a the torque reaction of the gearbox, transmitted through the housing.
- **L5** is a bending moment representing the weight of the first planetary stage of the gearbox, applied as a constant value at its shaft end.
- **L6** is the weight of the gearbox, modelled at its center of gravity.

The following table shows the load data for our study, which is applied to the SimPro model.

Load Component	**Min**	**Max**	**Mean**
Lateral F_x (kN)	-200	200	0
Thrust F_y (kN)	-100	1000	600
Vertical F_z (kN)	-1400	-1100	-1250
Tilt M_x (kNm)	-7100	12500	4200
Roll M_y (kNm)	-300	6700	3500
Yaw M_z (kNm)	-9500	8300	0

Table 3.3: Exemplary operating loads on the wind turbine

3.4 SimPro Analysis

3.4.1 Modelling

The drivetrain flexibility in SimPro is resolved using dynamic substructuring, also known as component mode synthesis. This method represents the elastic behaviour of the housing and shaft using a reduced set of structural modes, allowing the flexible assembly interaction between the rotor main shaft, bearings, and housing to be captured efficiently without the computational cost of a full flexible body solution. The SimPro models used for this purpose are the same models already maintained for every wind turbine project for the purpose of bearing life estimation, so no additional global modelling effort is required to perform the ring creep analysis presented here.

The simulation methodology follows a sequential two-step approach. First, the drivetrain assembly is simulated in SKF SimPro to extract the roller contact load distributions for each load combination. These distributions are then used directly as one of the boundary conditions in the ANSYS submodel described in Section 3.5, which resolves the resulting interfacial slip at the ring seat.

3.4.2 Simulations

The model is simulated in SimPro for each load component listed in Table 3.3 to obtain the resulting roller contact load distributions on both bearings, expressed as load maps in the radial plane of each bearing. The purpose of this screening is to reduce the number of parameters considered in the subsequent parametric study by identifying which load components produce a meaningful change in the roller load distribution.
If the roller contact load distribution for the minimum, mean, and maximum values of a given load component don't change significantly, the load component is considered to produce only marginal deviation within its studied range and is not carried forward. If the distributions vary significantly and do not overlap, the load component is identified as affecting the roller load distribution and is therefore considered to contribute significantly higher in the ring creep behaviour, motivating its inclusion in the parametric study in ANSYS. The resulting roller load distributions for all six load components are presented and discussed in Section 4.1.

3.4.3 Identification of Dominant Load Components

Of the six load components evaluated, Lateral, Thrust, and Vertical forces, together with the Roll moment on the rotor side bearing, show only marginal deviation in the roller load distribution within their studied ranges. The Tilt moment M_x and Yaw moment M_z, by contrast, produce roller load distributions that vary significantly and do not overlap across their studied range, on both the rotor side and gearbox side bearings. These two load components are therefore identified as the dominant contributors to ring creep behaviour and form the basis of the parametric study described below. The roller load distributions supporting this conclusion are shown in Section 4.1.

3.4.4 Tilt and Yaw Load Grid

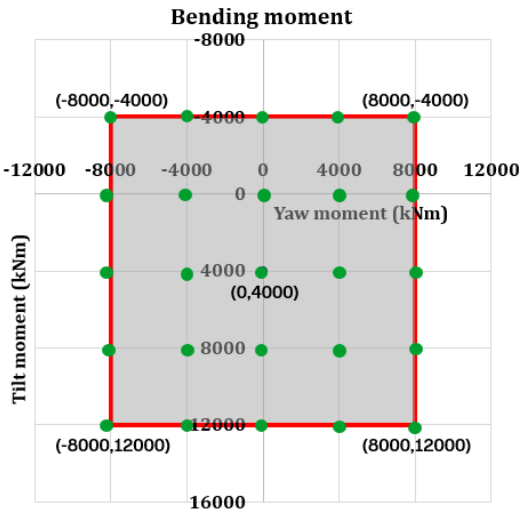

Figure 3.4: Grid of Tilt and Yaw load combinations studied

Based on the screening results, a grid of Tilt and Yaw moment combinations is defined to span the operational loading envelope, as shown in Figure 3.4. The grid spacing is chosen to provide sufficient resolution for constructing a continuous response surface while remaining computationally practical. Applying this spacing across the studied Tilt and Yaw ranges results in a grid of 25 load combinations (shown here as green dots on the grid). Each of the 25 load combinations is simulated in SimPro to obtain the corresponding roller contact loads for both bearings, which are exported and used as input for the nonlinear finite element analysis in ANSYS.

3.5 ANSYS Submodel

3.5.1 Submodel Architecture

The wind turbine assembly is divided into two submodels for the structural analysis, one representing the stationary parts of the assembly and one representing the rotating parts. This study focuses exclusively on the rotating submodel, comprising the main shaft with an adapter (red) and the inner races of the rotor side and gearbox side bearings, as shown in Figure 3.5. The adapter serves as a stiffener, which is important for the deformation of the hollow shaft to show realistic results for the ring creeping. The contact loads obtained from SimPro are applied to this submodel as the boundary condition representing the interaction with the stationary housing.

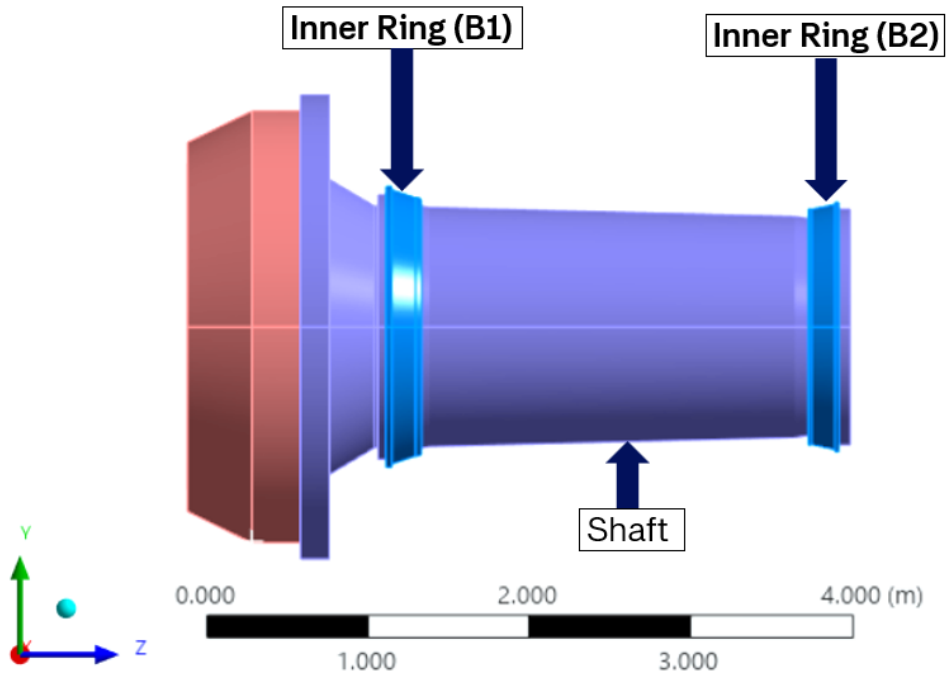

Figure 3.5: Ansys rotating submodel comprising the main shaft with adapter and inner rings

3.5.2 Mesh

The model is meshed using three-dimensional hexahedral elements across the circumference of all components, as shown in Figure 3.6. A linear order element formulation is used throughout, with an element size of 16 mm at the shaft-inner ring contact region. This discretisation results in a total of 283920 nodes and 231932 elements across the submodel for a mesh resolution of 300 elements around the shaft. The mesh comprises the main shaft and the inner races of the rotor side and gearbox side bearings. The selection of the mesh resolution used for the parametric study is based on a mesh sensitivity study, presented in Section 3.6.1.

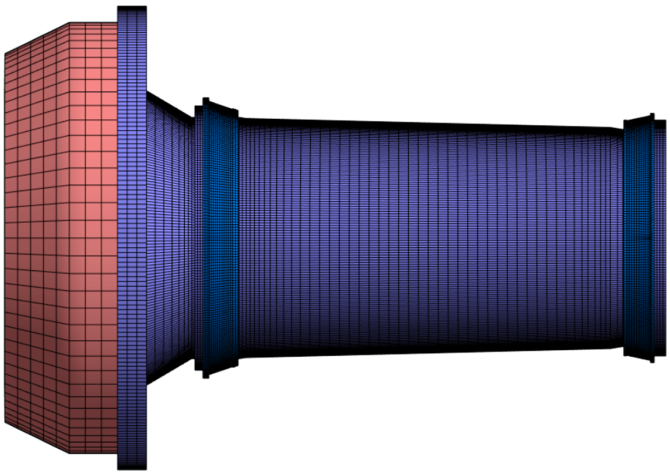

Figure 3.6: Meshed model in Ansys

3.5.3 Boundary Conditions and Line Load Simplification

The rigid body motions of the shaft are constrained at the rotor side. Since the shaft is physically rotating during operation, the loading on the inner ring raceway is instead rotated in the opposite direction, producing an equivalent relative motion at the contact interface while avoiding the numerical instabilities associated with large rigid body rotations of the shaft itself, as discussed in Section 2.5.2.

The contact between the rolling elements and the ring raceway is represented using uniform line loads applied across the inner race of both bearings, scaled according to the roller load magnitude obtained from SimPro. This simplification does not account for individual roller misalignments or contact length variation. Some deviation from the line load representation is therefore expected at the outer edges of the Tilt and Yaw load grid, where edge loading effects at the roller extremities become more significant. The interference fit is introduced in the submodel using the ANSYS CNOF contact offset parameter, set to 0.400 mm for the rotor-side bearing seat and 0.360 mm for the gearbox-side bearing seat, consistent with the diametral interference values specified in Section 3.2.3.1.

3.5.4 Load Sequencing and Quasi-Static Rotation

The simulation is executed using a custom APDL framework that manages a multi stage activation sequence to ensure numerical stability. The interference fit is first initialised, followed by activation of the seat friction, and finally the application of the rotating line loads representing the external loading condition.
The load rotation is performed over 2.1 revolutions in total. The first revolution, from 0 to 1 rev, allows the contact algorithm to settle from the initial interference fit and static loading condition into a stable cyclic response. The second revolution, from 1 to 2 rev, is then extracted for creep quantification, since the slip behaviour during this revolution is representative of the steady cyclic state. The remaining 0.1 revolutions are included for post-processing purposes. The angular increment used for the load rotation, together with the mesh resolution and contact stiffness, is determined through the sensitivity study presented in Section 3.6.

3.6 Sensitivity Study

Before performing the parametric study across the 25 load combinations defined in Section 3.4.4, a sensitivity study is conducted to determine the mesh resolution, contact stiffness factor, and angular increment that produce numerically converged creep predictions while remaining computationally efficient. The sensitivity study is performed for a single reference load case, chosen from experience with previous ring creep simulations of wind turbine main shaft bearings as a combination that typically shows significant ring creep and lies towards the outer edge of typical operational loads.

3.6.1 Mesh Resolution

The mesh resolution is varied in terms of the number of hexahedral elements around the circumference of the shaft, ranging from a finer mesh (480 elements) to progressively coarser meshes (360, 300, and 240 elements). The finest mesh (480 elements) is taken as the reference, and the objective of this study is to identify the coarsest mesh resolution whose effective creep result lies within an acceptable tolerance of this reference. The tangential slip response over one load rotation is compared across these mesh resolutions in terms of both local and global creep.

3.6.2 Contact Stiffness

In ANSYS, the penalty-based contact algorithm assigns a contact stiffness (controlled by the dimensionless factor FKN) that regulates the amount of numerical penetration permitted at the contact interface. When mesh resolution is varied with automatic stiffness scaling, finer meshes produce proportionally higher contact stiffness values, because the contact pressure is distributed over smaller element faces. This means that for coarser meshes, the default automatic contact stiffness may be insufficient to fully resolve the interface behaviour, underestimating the actual slip response. The contact stiffness sensitivity study therefore manually varies FKN at

the selected mesh resolution, with the objective of identifying the value at which the local creep response matches that of a finer reference mesh, confirming that the contact algorithm has resolved the interface behaviour correctly rather than being limited by numerical penetration.

3.6.3 Angular Increment

The angular increment used for the quasi-static load rotation is varied at the selected mesh resolution and contact stiffness. The objective of this study is to identify the largest angular increment for which the effective creep value remains within an acceptable tolerance of the finest reference case (1-degree increment), in order to minimise the computation time required for each of the 25 load combinations in the parametric study.

4

Results

This section presents the results of this study. The simulations in SimPro and ANSYS were carried out on a mobile workstation equipped with an Intel i7 13th Gen processor at 2.5 GHz, 64 GB of RAM, and a 500 GB solid state drive.

4.1 Roller Load Distribution Screening

Figures 4.1 through 4.6 present the roller contact load distributions obtained from SimPro for each of the six load components listed in Table 3.3, supporting the screening procedure and conclusions described in Section 3.4. For each load component, the minimum, mean, and maximum values are evaluated independently while the remaining five components are held at their mean values, and the resulting roller contact load maps for the rotor side and gearbox side bearings are compared.

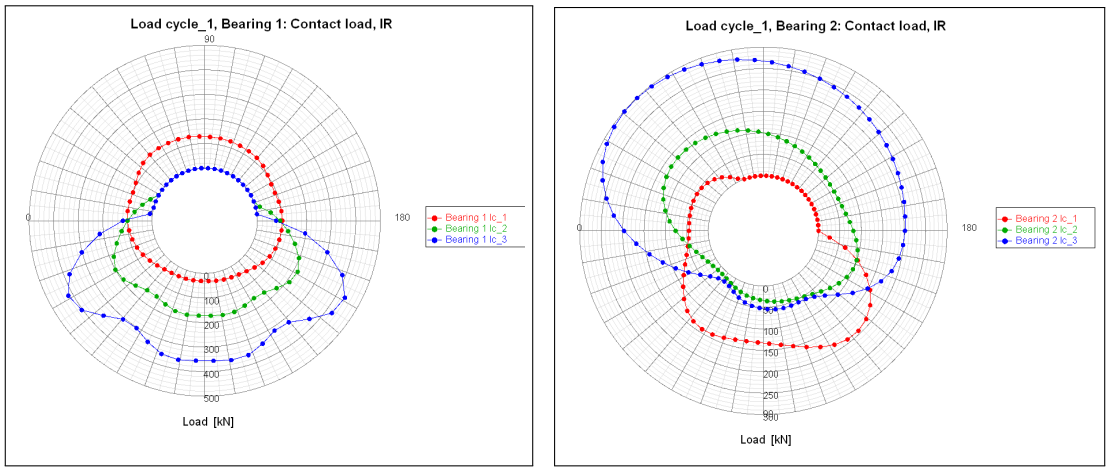

Figure 4.1: Roller load distribution as Minimum (Red), Mean (Green) and Maximum (Blue) values for the Tilt moment on the rotor side and gearbox side bearings

The Tilt moment produces roller load distributions that vary significantly across its studied range on both bearings, with the shape of the distribution changing substantially between the minimum, mean, and maximum values, as shown in Figure 4.1. The Tilt moment is therefore identified as a dominant contributor to the roller load distribution and is carried forward to the parametric study.

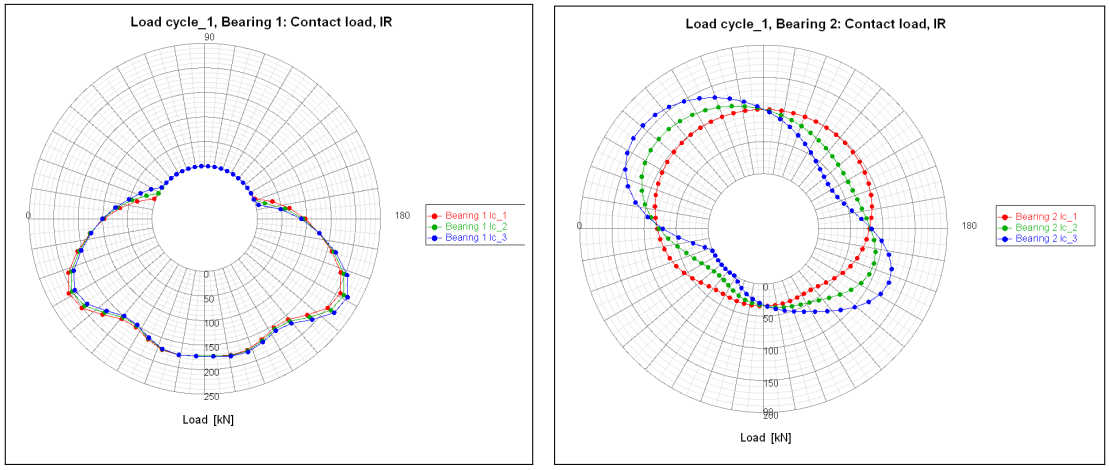

Figure 4.2: Roller load distribution as Minimum (Red), Mean (Green) and Maximum (Blue) values for the Roll moment on the rotor side and gearbox side bearings

The Roll moment (torque) produces roller load distributions on the rotor side bearing that closely coincide across the studied range. On the gearbox side bearing, the distributions vary more noticeably, as shown in Figure 4.2. As this study focuses on the rotor side bearing, the Roll moment is not carried forward to the parametric study.

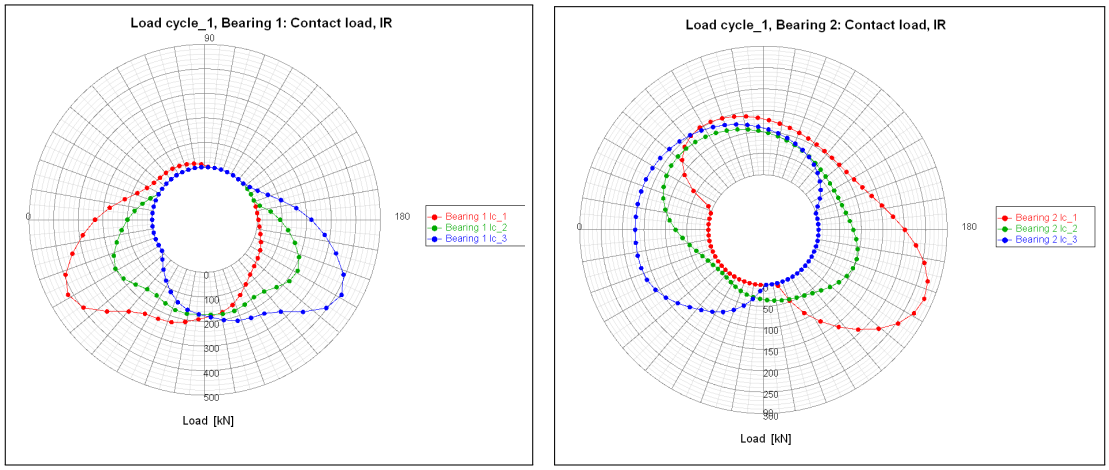

Figure 4.3: Roller load distribution as Minimum (Red), Mean (Green) and Maximum (Blue) values for the Yaw moment on the rotor side and gearbox side bearings

The Yaw moment, like the Tilt moment, produces roller load distributions that vary significantly across its studied range on both bearings, with the distribution shape changing substantially between the minimum, mean, and maximum values, as shown in Figure 4.3. The Yaw moment is therefore also identified as a dominant contributor to the roller load distribution.

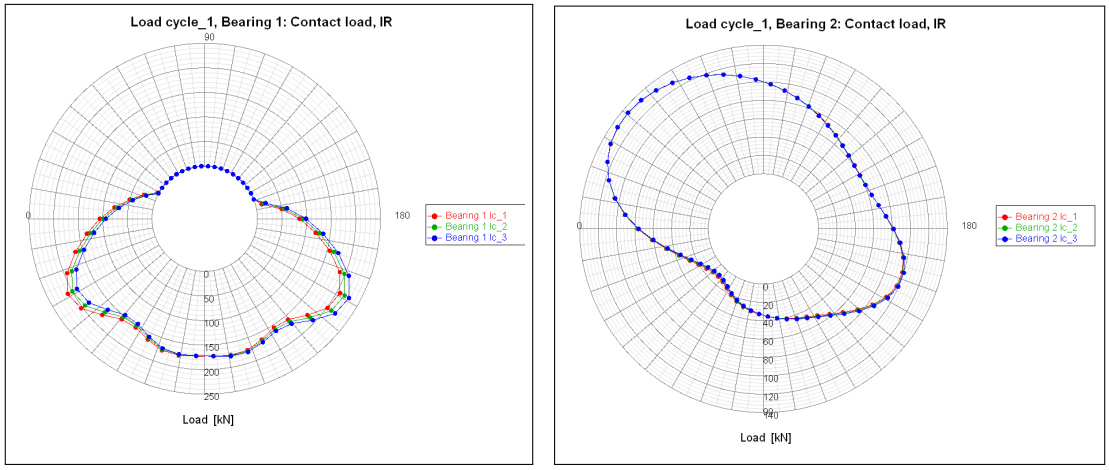

Figure 4.4: Roller load distribution as Minimum (Red), Mean (Green) and Maximum (Blue) values for the Lateral load component on the rotor side and gearbox side bearings

For the Lateral load component, the roller load distributions remain concentric and overlapping across the studied range on both bearings, as shown in Figure 4.4. Consistent with the screening criterion in Section 3.4.2, this load component is identified as producing only marginal deviation in the roller load distribution.

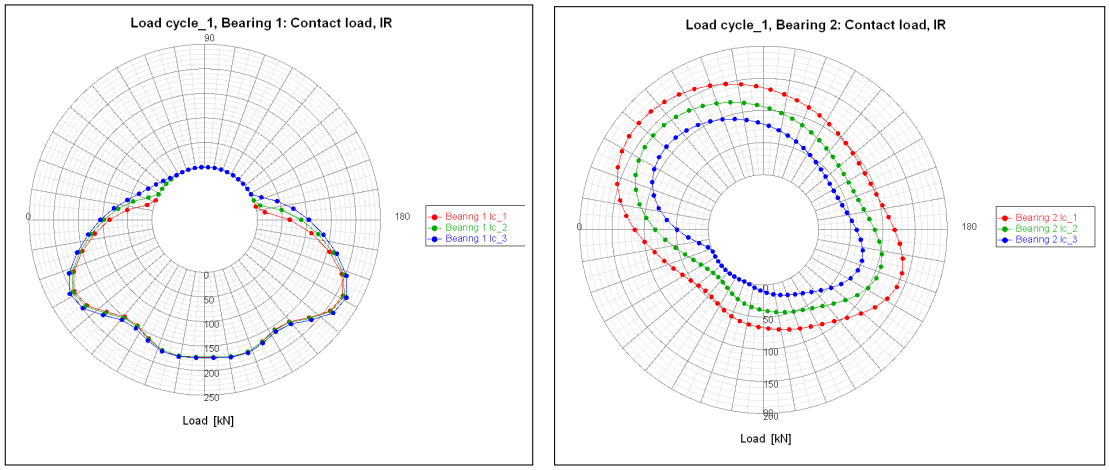

Figure 4.5: Roller load distribution as Minimum (Red), Mean (Green) and Maximum (Blue) values for the Thrust load component on the rotor side and gearbox side bearings

The Thrust load component similarly produces overlapping roller load distributions on the rotor side bearing, and on the gearbox side bearing the distributions remain concentric, as shown in Figure 4.5. This load component is therefore also identified as producing only marginal deviation within its studied range.

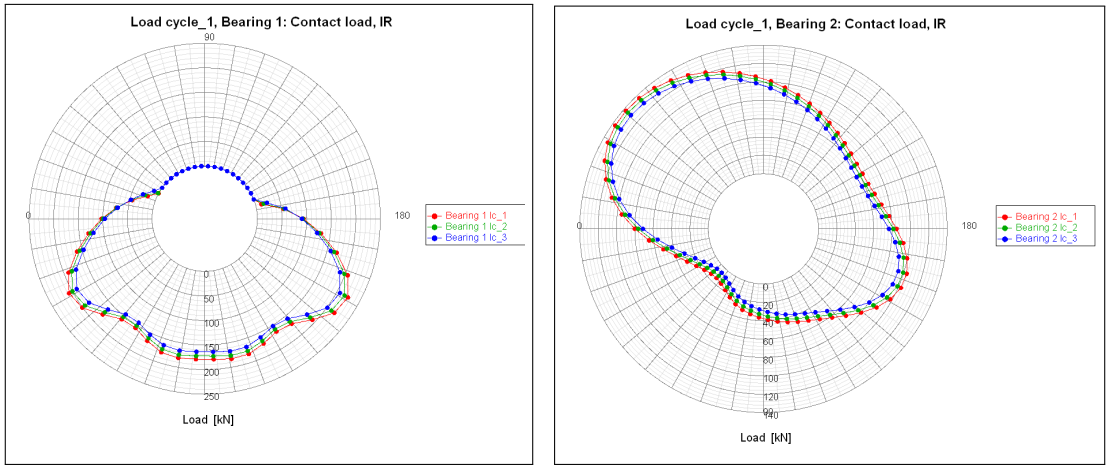

Figure 4.6: Roller load distribution as Minimum (Red), Mean (Green) and Maximum (Blue) values for the Vertical load component on the rotor side and gearbox side bearings

The Vertical load component produces only minimal changes to the roller load distribution on both bearings, as shown in Figure 4.6, and is likewise identified as producing only marginal deviation within its studied range.
On the basis of these results, the Tilt moment M_x and the Yaw moment M_z are identified as the dominant load components affecting the roller load distribution on the rotor side bearing, consistent with the conclusion stated in Section 3.4.3. These two load components form the basis of the grid of 25 load combinations shown in Figure 3.4 and used as input for the parametric study in ANSYS.

4.2 Sensitivity Study

This section presents the results of the sensitivity study described in Section 3.6, in which the mesh resolution, contact stiffness factor, and angular increment used for the parametric study are determined. All results in this section correspond to the reference load case at Tilt moment $M_x = 8000$ kNm and Yaw moment $M_z = 4000$ kNm, with the remaining load components held at the estimated mean values given in Table 3.3.
Two slip quantities are used throughout this section and reported in all slip curve figures. *Local creep* (labelled "ref" in figure legends) is the relative tangential displacement between the inner ring bore and the shaft at a single reference node on the circumference, evaluated as a continuous function of load vector rotation angle ϕ, as defined in Section 2.4.1. *Global creep* (labelled "tot") is the circumferential average of the local creep across all nodes on the ring at each load step, as defined in Section 2.4.1.

4.2.1 Mesh Resolution

The mesh resolution is varied in terms of the number of elements around the circumference of the shaft, ranging from a fine mesh of 480 elements to a coarser mesh

of 240 elements. Figure 4.7 compares the tangential slip response over one load rotation in terms of global creep (tot) and local creep (ref) for each mesh resolution.

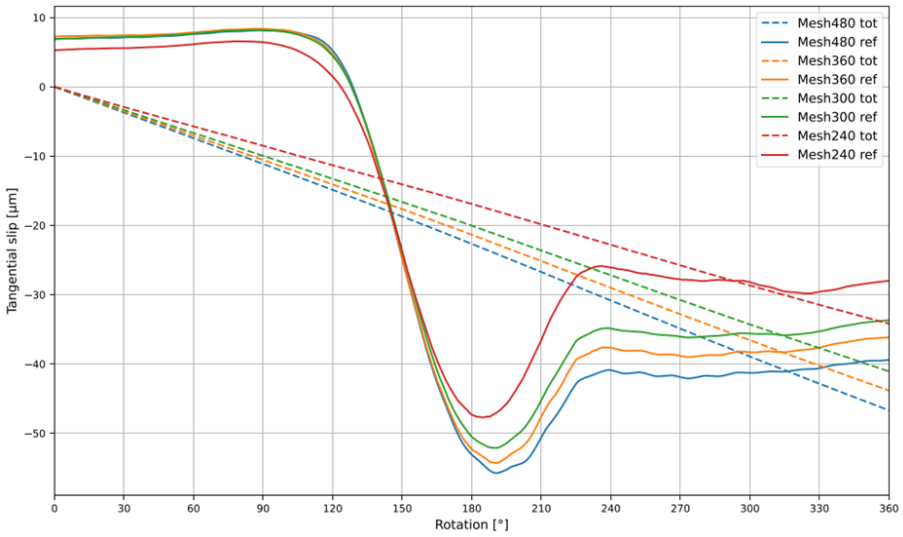

Figure 4.7: Tangential slip response for varying mesh resolution

Across all cases the slip response follows the same overall shape: starting near zero, dropping sharply between approximately 150 and 180 degrees of rotation, recovering toward the final value by 360 degrees, with a secondary local feature near 270 degrees. Figure 4.8 summarises the computation time, using 20 CPU cores, and the resulting relative tangential creep for each mesh resolution.

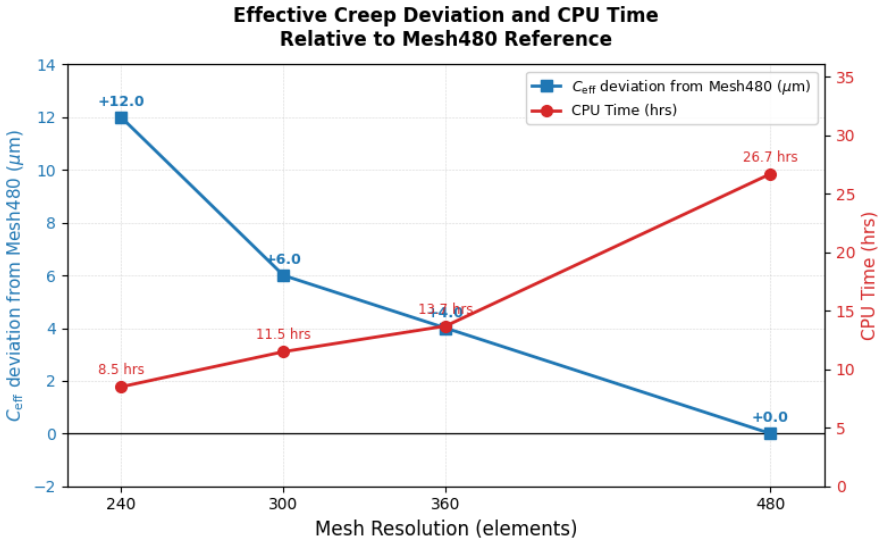

Figure 4.8: Mesh resolution with corresponding CPU time and relative creep

Figure 4.8 shows the effective creep deviation of each mesh resolution relative to the 480-element reference, together with the corresponding computation time. The 360-element mesh deviates by $+4\,\mu$m (10 %), requiring 13.7 hrs, and the 300-element

mesh deviates by +6 μm (15 %), requiring 11.5 hrs both substantially less than the 26.7 hrs of the reference while maintaining an acceptable level of accuracy. The 240-element mesh deviates by +12 μm (30 %), indicating that this resolution is no longer an acceptable approximation of the reference result. A mesh resolution of 300 elements is therefore selected for the parametric study, providing a favourable balance between result accuracy and computational cost.

4.2.2 Contact Stiffness

In ANSYS, the penalty-based contact algorithm automatically scales the contact stiffness with element size: finer meshes produce proportionally higher stiffness values because the contact pressure acts over smaller element faces. Reducing mesh resolution therefore also reduces the automatic contact stiffness, which can cause the solver to underestimate interfacial slip. Manually increasing the contact stiffness factor FKN at the selected coarser mesh compensates for this effect and allows the slip response to match that of the finer reference mesh, achieving comparable accuracy at substantially lower computational cost. If FKN is set too high relative to the mesh resolution, solver convergence difficulties may arise; however, this was not encountered in the present study.
Figure 4.9 shows the tangential slip curves for FKN values of 1.0, 1.2, 1.4, and 1.6 at the selected 300-element mesh, alongside the 480-element reference at FKN = 1.0. Both global slip (tot, dashed) and local slip (ref, solid) are shown.

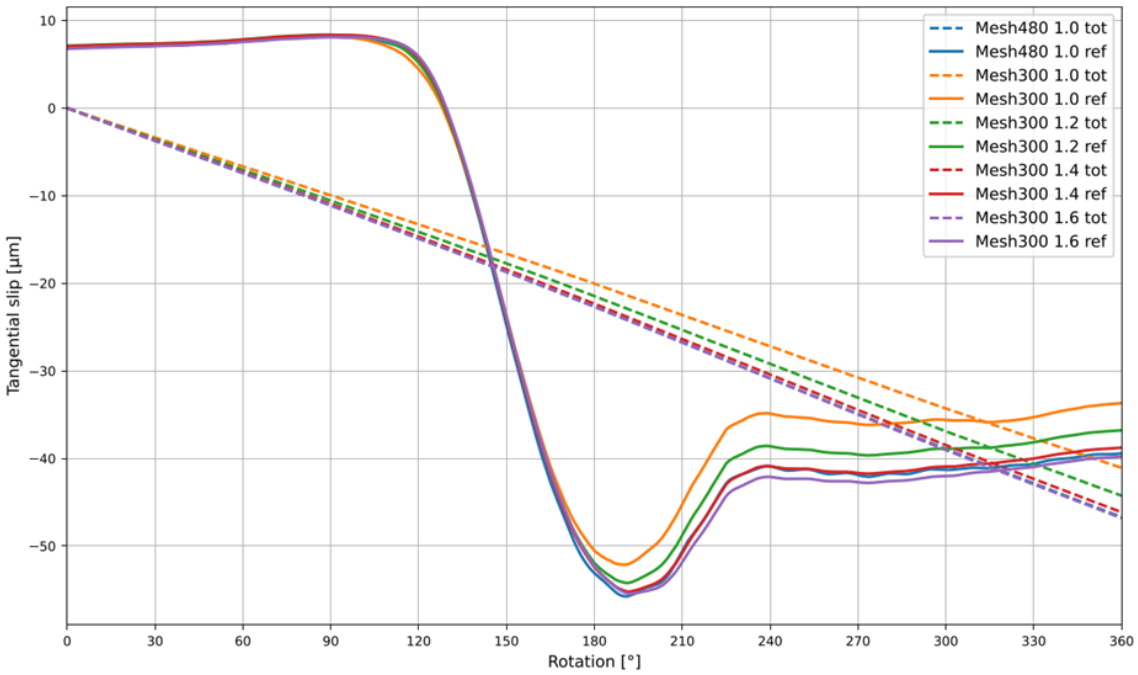

Figure 4.9: Tangential slip response for varying contact stiffness

At FKN = 1.0 with the 300-element mesh, the local slip curve deviates noticeably from the reference, overestimating slip in the latter half of the rotation by approximately 8 to 10 μm. Once FKN is increased to 1.2, the 300-element curves collapse

onto a tight band and remain stable through FKN = 1.6, indicating that the contact algorithm has resolved the interface behaviour independently of further stiffness increases. The 480-element reference at FKN = 1.0 also falls within this band, confirming that the deviation at FKN = 1.0 on the 300-element mesh is attributable to the reduced automatic contact stiffness rather than to mesh resolution itself. A contact stiffness factor of FKN = 1.5 is selected for the parametric study, as a value comfortably within this matching range.

4.2.3 Angular Increment

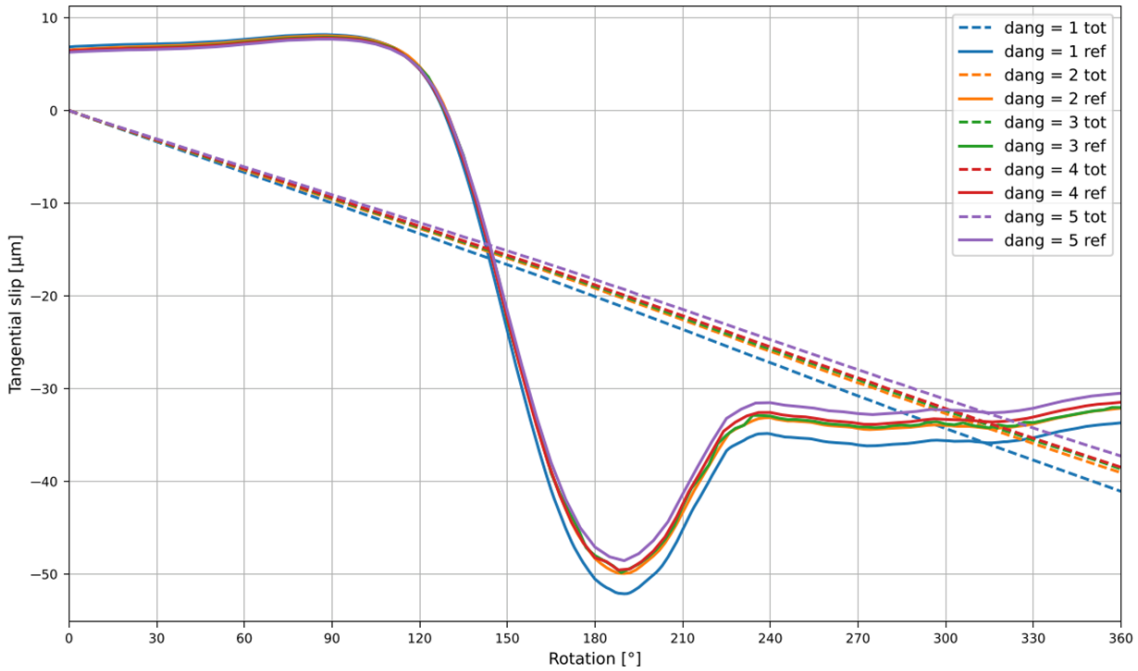

Figure 4.10: Tangential slip response for varying angular increment

Figure 4.10 shows the tangential slip curves for angular increments of 1, 2, 3, 4, and 5 degrees, at the selected mesh resolution of 300 elements and contact stiffness factor of 1.0, as it was done in parallel with the contact stiffness study.
The objective of this study is to determine the largest angular increment for which the effective creep value remains converged, in order to minimise the computation time required for each of the 25 load combinations in the parametric study.
The 1 degree increment produces a local slip curve that sits approximately 5 to 6 micrometres below the remaining cases in the latter half of the rotation, attributed to the finer angular stepping resolving additional micro slip reversals that coarser increments smooth over. From 2 degrees onward, the local slip curves converge tightly and remain consistent through 5 degrees, with differences in the final effective creep value of less than 2 micrometres.
Figure 4.11 summarises the computation time, using 10 CPU cores, and the resulting total creep for each angular increment.

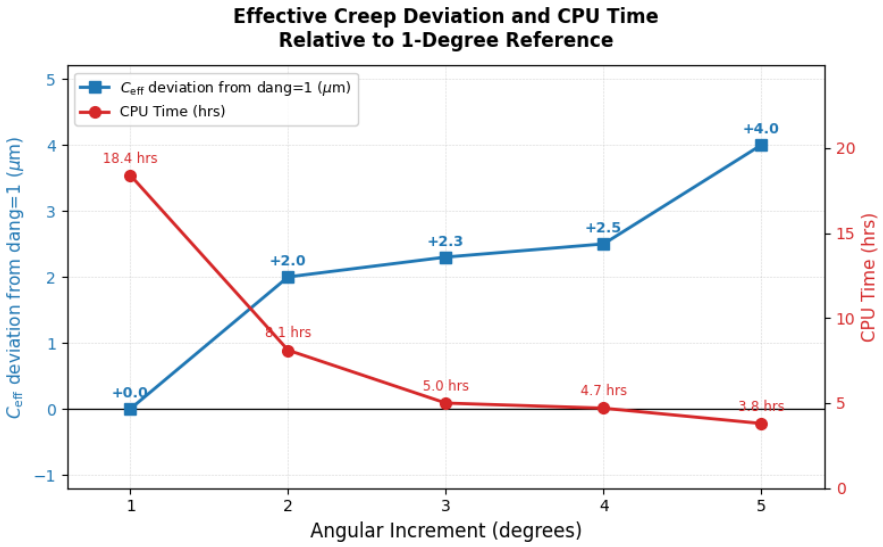

Figure 4.11: Angular increment with corresponding CPU time and Relative creep

Figure 4.11 shows the effective creep deviation of each angular increment relative to the 1-degree reference, together with the corresponding computation time. The 1-degree increment is the most accurate but requires 18.4 hrs. At 2 degrees the deviation is $+2.0\,\mu$m (4.9 %), with the computation time reduced to 8.1 hrs. The 3- and 4-degree increments show deviations of +2.3 and $+2.5\,\mu$m respectively, remaining on the order of $2\,\mu$m from the reference; the stick-slip transition is still resolved at these increments, though the waveform is increasingly smoothed by the coarser stepping. At 5 degrees the deviation grows to $+4.0\,\mu$m (9.8 %), indicating that the angular resolution is no longer sufficient to adequately capture the stick-slip transition at each load step. An angular increment of 4 degrees is therefore selected for the parametric study, reducing computation time to 4.7 hrs, a 75 % reduction relative to the 1-degree reference with a creep deviation of $+2.5\,\mu$m.

4.2.4 Summary of Selected Parameters

Table 4.1 summarises the mesh resolution, contact stiffness factor, and angular increment selected for the parametric study based on the sensitivity study presented above, together with the corresponding computation time, memory usage, and number of CPU cores used.

Parameter	Reference	Selected
Mesh resolution	480 elements	300 elements
Contact stiffness (FKN)	1.0	1.5
Angular increment	1 degree	4 degrees
Computation time	∼26.7 hrs	∼4.7 hrs
CPU cores	20	10

Table 4.1: Selected numerical parameters for the parametric study, compared against the reference configuration

4.3 Parametric Study

Both response surfaces for effective creep and accumulated slip are generated from the grid of 25 load combinations defined in Section 3.4.4, using the mesh resolution, contact stiffness, and angular increment selected in Section 4.2. The discrete results are interpolated using Ordinary Kriging with a Gaussian model, as described in Section 2.5.3. In both Figures 4.12 and 4.13, the Tilt moment axis is inverted, so that the top of the plot corresponds to the most negative Tilt values, M_x approximately -4000 kNm, and the bottom to the largest positive values, M_x approximately 12000 kNm. The sign convention for effective creep follows the post processing framework described in Section 2.4.2: a positive value of C_{eff} indicates migration in the same rotational sense as the applied load rotation, and a negative value indicates migration in the opposing sense.

4.3.1 Effective Creep

Figure 4.12 shows how the net ring drift per revolution varies across the Tilt and Yaw loading space. Three distinct regions are visible.

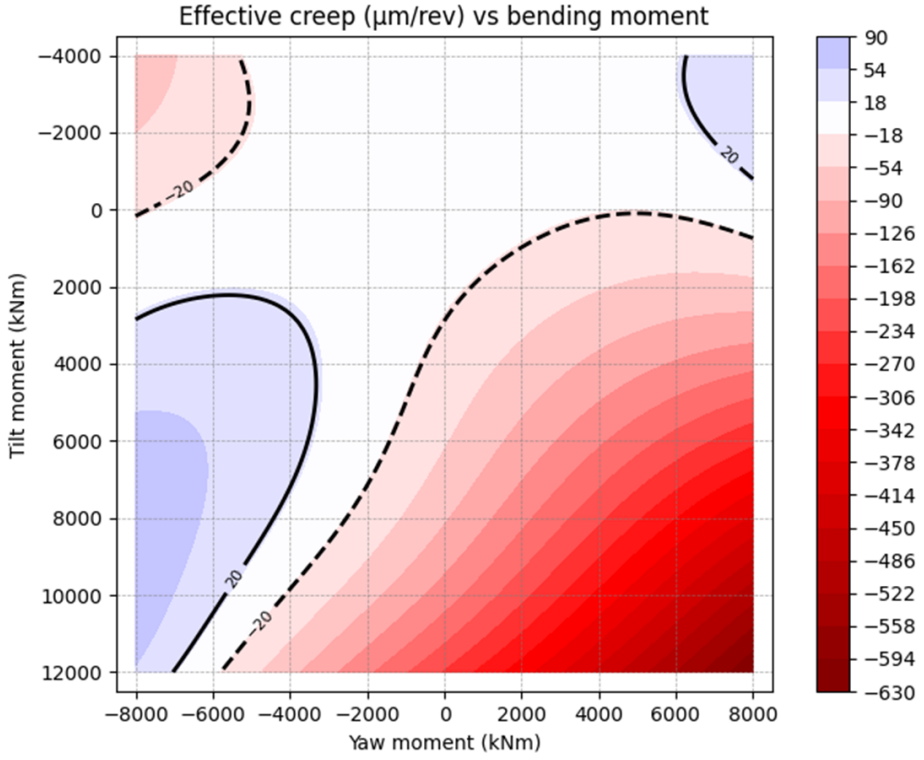

Figure 4.12: Effective creep as a function of Tilt and Yaw moment

At high positive Tilt, above approximately 12000 kNm, combined with positive Yaw, above approximately 8000 kNm, the effective creep reaches values of up to approximately -630 micrometres per revolution. In this region, the bending induced

ovalization of the bearing seat overcomes the frictional capacity of the interference fit, and the ring migrates continuously in the opposing rotational sense to the applied load rotation.
A central band, bounded by the dashed contours at ±20 micrometres per revolution, represents a region of stable micro slip, where the interference fit retains sufficient frictional capacity to prevent net ring migration. This band narrows and shifts toward more negative Yaw values as the Tilt moment increases.
At positive Tilt and large negative Yaw, below approximately −6000 kNm, the ring migrates in the same rotational sense as the applied load rotation, reaching values of up to approximately +90 μm per revolution, as the structural deformation of the housing reinforces slip in the positive circumferential direction. It is also notable that at Yaw moments below approximately −6000 kNm, even at moderate to high Tilt levels, the net effective creep is near zero, indicating that these load combinations produce a nearly symmetric slip cycle with negligible net displacement per revolution. For Tilt moments exceeding approximately 8000 kNm, the entire positive Yaw domain lies beyond the −20 μm per revolution threshold, indicating that a sufficiently high Tilt moment alone is capable of driving the ring into the macro-wandering regime, independent of the Yaw moment.

4.3.2 Accumulated Slip

Figure 4.13 shows the accumulated slip, corresponding to the total frictional work dissipated at the ring seat interface per revolution, as defined in Section 2.4.3. The topography of this response surface is markedly different from the effective creep surface, indicating that it captures a distinct aspect of the interface behaviour.

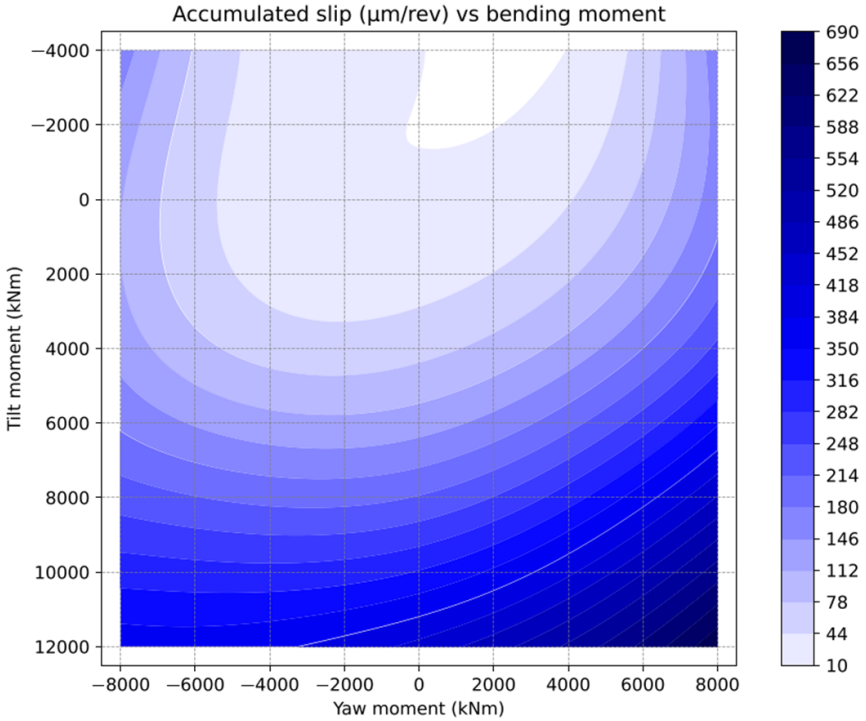

Figure 4.13: Accumulated slip as a function of Tilt and Yaw moment

The highest accumulated slip, reaching approximately 690 m per revolution, occurs at large negative Tilt, around $M_x = -4000\,\text{kNm}$, combined with large negative Yaw, below approximately $M_z = -4000\,\text{kNm}$ the upper-left region of the plot.
This is the same region where the effective creep is near zero, indicating that the ring undergoes substantial oscillatory back-and-forth motion within each load cycle without corresponding net migration.
In the macro-wandering region at high positive Tilt and positive Yaw, where effective creep reaches its maximum magnitude, the accumulated slip converges toward the magnitude of the effective creep, since the ring migrates continuously in one direction and the reversible oscillatory component of the motion diminishes accordingly.
The fact that the two maxima occur in distinctly different regions of the loading space confirms that an assessment based on effective creep alone would not fully characterise the ring seat condition across the operational loading envelope.

4.4 Operational Load Distribution and Annual Creep Accumulation

4.4.1 Operational Load Distribution

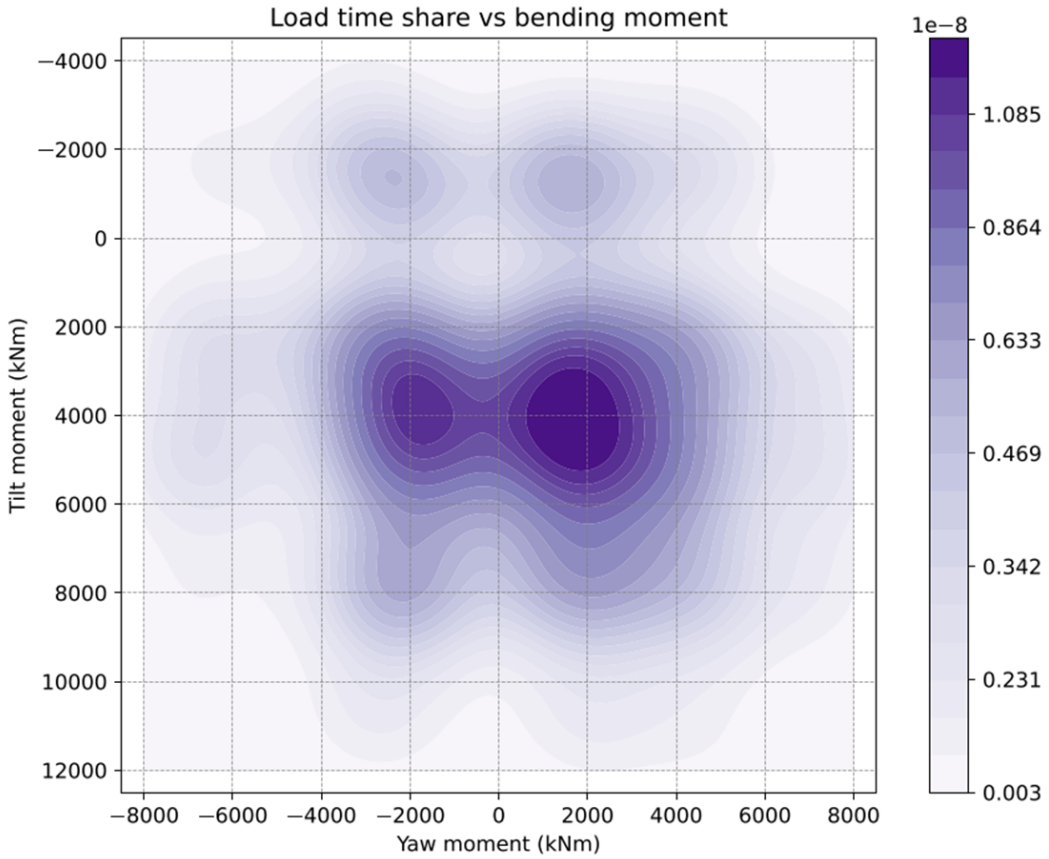

Figure 4.14: Recorded operational load distribution as a function of Tilt and Yaw moment

To relate the parametric finite element results to real operating conditions, the response surfaces obtained in Section 4.3 are combined with a generic wind turbine load history using the approaches described in Section 2.5.4. Each operating point in the Tilt and Yaw load history is weighted by its associated creep contribution and normalised by the unweighted sampling density of the load history, yielding a map of annual creep accumulation that accounts for both the severity of creep at a given load combination and how often that load combination occurs in operation.

Figure 4.14 shows that the turbine spends most of its operational life at moderate Tilt moments, between approximately 3000 and 5000 kNm, and low to moderate Yaw moments, within approximately ±3000 kNm. The distribution has two characteristic density peaks at approximately M_z equal to ±2000 kNm, reflecting the bidirectional nature of wind-induced yaw excitation during normal power production. Beyond approximately ±4000 kNm in Yaw and approximately 8000 kNm in Tilt, the density drops sharply, confirming that extreme bending moment combinations are rarely encountered in service.

4.4.2 Time Share Distribution

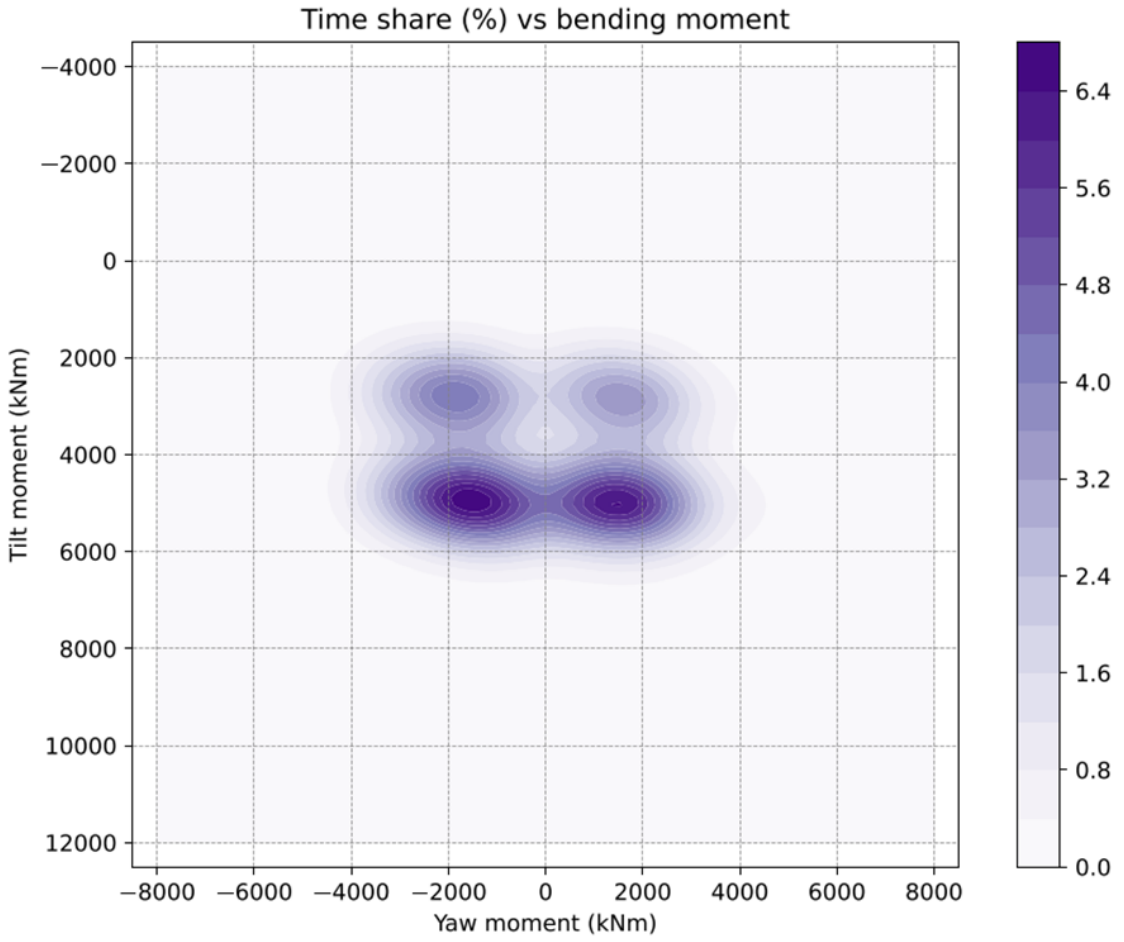

Figure 4.15: Percentage time share as a function of Tilt and Yaw moment

Figure 4.15 presents the percentage of operational time spent at each Tilt and Yaw load combination across the full recorded load history. The map is produced using a kernel density estimate of the load occurrence distribution, weighted by the time share at each classified load point and normalised by the unweighted sampling density. This produces a scaled distribution plot whose shape is identical to a kernel density estimate of the time-weighted load distribution, but whose values are scaled so that the colourbar reads directly in percentage time share per load region rather than in probability density units.

The distribution reveals four distinct regions arranged symmetrically about the Tilt axis at approximately 4000 to 5000 kNm. Two inner regions, centred at approximately $M_z = -2000$ kNm and $+2000$ kNm, are the most densely populated, each reaching a peak time share of approximately 6.4 % per load bin. Two outer regions, located at approximately $M_z = -4000$ kNm and $+3000$ kNm, show a visibly lower but non-negligible time share. Outside these four regions the time share drops sharply to near zero; extreme Tilt moments above approximately 7000 kNm and large Yaw excursions beyond approximately ± 5000 kNm account for only a negligible fraction of total operating time.

4.4.3 Annual Creep Accumulation

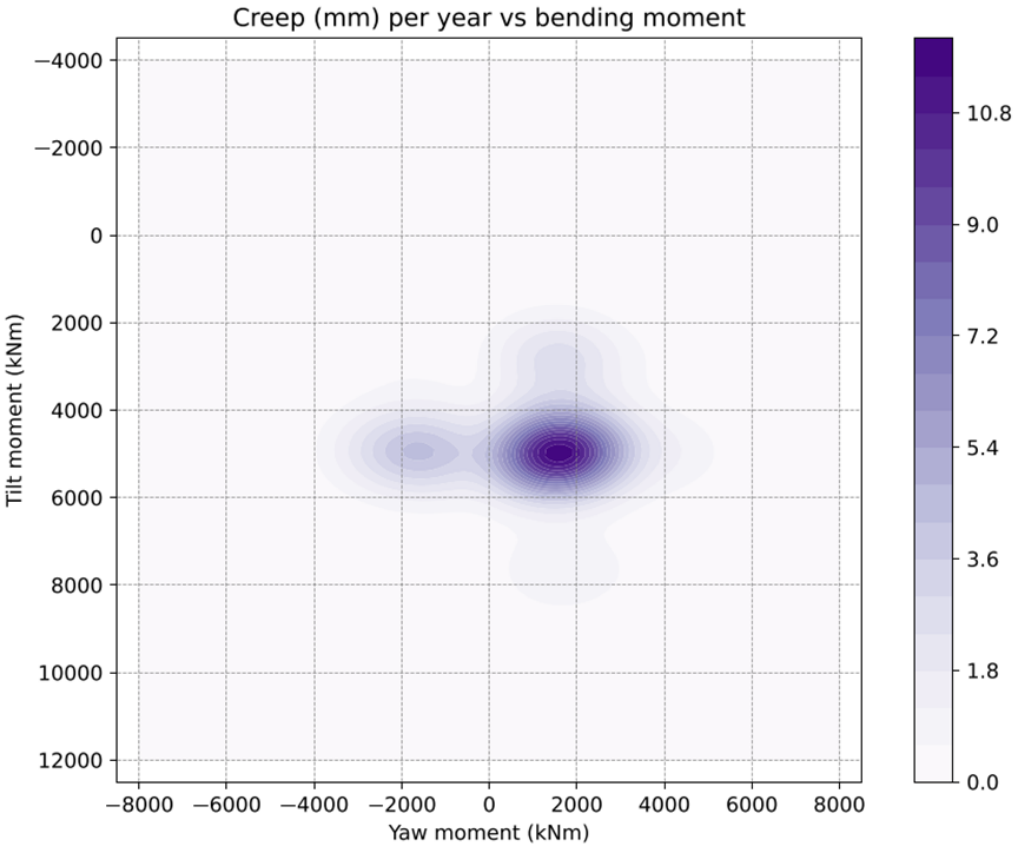

Figure 4.16: Annual creep accumulation as a function of Tilt and Yaw moment

Figure 4.16 shows the annual creep accumulation map. The map is produced using the same kernel density normalisation approach as the time share distribution: a kernel density estimate of the load occurrence distribution is weighted by the annual creep contribution at each classified load point and normalised by the unweighted sampling density, yielding a scaled distribution plot whose colourbar reads directly in millimetres of ring migration per year. The shape of the map is therefore analogous to a kernel density plot of the creep-weighted load distribution, but scaled to physically meaningful units rather than probability density. Each colourbar value represents the conditional mean annual creep contribution at that Tilt and Yaw location, accounting for both the severity of ring creep at that load combination and how frequently the turbine operates there, integrated across all classified load conditions in the recorded load history.

The map reveals an asymmetry that is not visible in the time share distribution alone. The region at approximately $M_z = +2000\,\text{kNm}$ dominates the annual creep accumulation, reaching values of up to approximately 10.8 mm per year. The corresponding region at approximately $M_z = -3000\,\text{kNm}$ at the same Tilt level contributes only approximately 5 to 6 mm per year, roughly half as much, despite being visited with comparable frequency. This asymmetry follows directly from the effective creep response surface: positive Yaw combined with moderate to high Tilt lies closer to the macro-wandering threshold, while negative Yaw at the same Tilt levels remains in a lower-severity region of the creep response surface.

The central finding from this comparison is that the most damaging operating region and the most frequently visited operating region are essentially coincident. Ring creep accumulation in this configuration is therefore driven primarily by normal power production loading rather than by extreme or rare load events. This has a direct engineering implication: managing ring creep in this turbine configuration requires attention to the interference fit specification and housing stiffness at normal operational loads, not only at extreme design loads.

5

Conclusion

This study presented an exemplary FEA-based case study, developed within SKF AECC, to visualise and quantify the influence of aerodynamic load components on structure-induced ring creep in a generic multi-megawatt wind turbine main shaft bearing arrangement. A multi-scale simulation framework was used, coupling system-level bearing load extraction in SKF SimPro using dynamic substructuring with a non-linear, quasi-static finite element submodel in ANSYS, in which the contact load vector was rotated across the inner ring raceway rather than rotating the shaft itself.

A roller load distribution screening across six load components showed that the Lateral, Thrust, and Vertical forces, together with the drivetrain torque on the Rotor Side bearing, produced only marginal deviation in the roller load distribution within their studied ranges. The Tilt and Yaw moments, by contrast, produced roller load distributions that varied significantly and did not overlap across their studied ranges on both bearings, and were therefore identified as the dominant contributors to ring creep behaviour. This outcome motivated a parametric study comprising a grid of 25 Tilt and Yaw moment combinations spanning the operational loading envelope.

Prior to the parametric study, a sensitivity study established the mesh resolution, contact stiffness factor, and angular increment required for numerically acceptable creep predictions. A mesh resolution of 300 elements around the shaft circumference, a contact stiffness factor of 1.5 to match the slip response of the 480-element reference mesh, and an angular increment of 4 degrees were found to produce effective creep results within approximately $2.5\,\mu$m of the 1-degree reference while reducing total computation time by approximately 75 %, providing a practical basis for completing the 25-case parametric study within an acceptable computational budget.

The parametric study revealed a strongly non-linear relationship between the applied Tilt and Yaw moments and the resulting ring creep behaviour. The maximum effective creep observed across the studied loading envelope was approximately $-630\,\mu$m per revolution, occurring at high positive Tilt, approximately $M_x = 12000\,\text{kNm}$, combined with positive Yaw, approximately $M_z = 8000\,\text{kNm}$, where the bending-induced ovalization of the bearing seat overcame the frictional capacity of the interference fit and resulted in continuous ring migration in the opposing rotational sense to the applied load rotation. The maximum accumulated slip observed was approximately $690\,\mu$m per revolution, occurring at large negative Tilt, around $M_x = -4000\,\text{kNm}$, combined with large negative Yaw, below approximately $M_z = -4000\,\text{kNm}$ – a region in which the effective creep is near zero, indicating that the ring undergoes substantial oscillatory back-and-forth motion within each load

cycle without corresponding net migration. The fact that the two maxima occur in distinctly different regions of the loading space confirms that the two metrics capture separate aspects of the ring seat interface behaviour, and that an assessment based on effective creep alone would not fully characterise the ring seat condition across the operational loading envelope.

Integration of the parametric response surfaces with a recorded operational load history showed that the turbine spends the majority of its operational life at moderate Tilt moments and low to moderate Yaw moments, with the time share distribution exhibiting a structure of four regions reflecting the bidirectional nature of wind-induced yaw excitation. When the response surfaces were combined with this operational load distribution using a scaled kernel density approach, in which the colourbar of each map reads directly in physical units of percentage time share and millimetres per year respectively rather than in probability density units, the annual creep accumulation reached its highest value of approximately 10.8 mm per year at a Tilt moment of approximately 4000 to 5000 kNm and a Yaw moment of approximately +2000 kNm. Critically, the most damaging operating region and the most frequently visited operating region were found to be essentially coincident, indicating that ring creep accumulation in this configuration is driven primarily by normal power production loading rather than by extreme or rare load events. Consequently, effective mitigation of ring creep in this turbine configuration requires attention to the interference fit specification and housing stiffness at normal operational loads, not only at extreme design loads.

It is important to note that all results are specific to the structural stiffness of the generic housing and shaft geometry used, including the deliberately reduced housing wall thickness. A change in the structural stiffness of either component would alter the distribution of bending-induced ovalization at the bearing seat and would therefore shift the response surfaces and the resulting annual creep accumulation map. The results should accordingly be interpreted as specific to this configuration rather than as generally applicable values.

Overall, this study demonstrates that the multi-scale simulation framework developed at SKF AECC provides a computationally efficient and practical means of predicting ring creep behaviour across the operational loading envelope of a wind turbine main shaft bearing. By combining a load component screening, a parametric finite element study, and an operational load weighting approach, the framework enables the prediction of ring creep risk in operation in a manner analogous to established bearing life prediction methodology, fulfilling the purpose set out at the beginning of this study.

6
Future Work

The following directions for future work are proposed based on the scope and findings of this study.

The parametric study and the resulting response surfaces were obtained exclusively for the Rotor Side bearing. The roller load distribution screening showed that the drivetrain torque produces a more significant variation on the Gearbox Side bearing than on the Rotor Side bearing. Future work should therefore repeat the parametric study for the Gearbox Side bearing, including a screening of all six load components for this bearing, since the dominant load components and the resulting response surfaces may differ from those identified for the Rotor Side bearing.

As the results of this study are dependent on the structural stiffness of the housing and shaft, future work should extend the parametric framework to include the stiffness of these components as additional study parameters. By systematically varying the housing wall thickness and shaft stiffness and repeating the parametric study for each configuration, design recommendations could be developed that relate structural stiffness directly to ring creep risk, providing a basis for stiffness-based design guidance at the drivetrain design stage.

Finally, the present study uses classified static load cases derived from SimPro rather than a dynamic load time series. Future work should investigate the effect of combined, simultaneously varying load components on ring creep, to assess whether the dynamic interaction between load components introduces additional contributions to ring creep that are not captured by the statically and independently varied load cases considered in this study.

Bibliography

.

[1] D. Billenstein, M. Neidnicht, et al., "Advanced, numerical simulation of the bearing ring creeping failure mode and comparison with experimental test results for rotor main bearing applications," in *Proc. CWD 2023*, Aachen, Germany, 2023.

[2] D. Billenstein, M. Neidnicht, et al., "Simulative and Experimental Investigation of the Ring Creeping Damage Mechanism Considering the Training Effect in Large-Sized Bearings," *Machines*, vol. 11, no. 5, p. 543, 2023.

[3] P. Grosse and H. Kyling, "Numerical simulation of ring creep on a wind turbine main shaft," *Forschung im Ingenieurwesen*, vol. 89, no. 19, 2025.

[4] A. Sadeghi et al., "A Review of Rolling Contact Fatigue," *Journal of Tribology*, vol. 131, no. 4, 2009.

[5] J. Kirsch and H. Kyling, "Optimized cast components in the drive train of wind turbines and inner ring creep in the main bearing seat," *Forschung im Ingenieurwesen*, vol. 85, no. 2, pp. 199–210, 2021.

[6] Deutsches Institut für Normung e.V. (Ed.), "DIN 7190-1:2017-02 Interference Fits (Part 1: Calculation and Design Rules for Cylindrical Self-Locking Press-fits)," *Beuth-Verlag*, Berlin, Germany, 2017.

[7] A. Maiwald, "Specific creeping phenomena of roller bearings used in lightweight constructions," in *Proc. 4th Bearing World*, Würzburg, Germany, July 2022.

[8] H. Carstens, C. Tremmel, and S. Tremmel, "FE Simulations of Irreversible Relative Movements (Creeping) in Rolling Bearing Seats - Influential Parameters and Remedies," in *Proc. International Association of Engineers (IAENG) World Congress on Engineering and Computer Science*, San Francisco, USA, vol. II, pp. 1030–1035, Oct. 2013.

[9] M. Göbbel, J. Neitz, and G. Jacobs, "Simulation based prediction of ring creep on a planetary bearing of a 1MW wind turbine gearbox," in *Proc. Conference on Wind Energy Drivetrains (CWD 2023)*, RWTH Aachen University, Germany, 2023.

[10] K. Toda, T. Matsubara, and H. Kozuka, "Development of Anti-Creep Ball Bearing for Outer Ring Caused by Outer Ring Strain," *JTEKT Engineering Journal (English Edition)*, no. 1014E, pp. 60–65, 2017.

[11] Fraunhofer IWES, "WEA-RiWa: Prediction of the ring creep tendency of rolling bearings in wind turbines," *Fraunhofer Institute for Wind Energy Systems Research Report*, Bremerhaven, Germany, Project Reference No. 03EE3051, 2024.

[12] A. Jacob, "Measurement and modelling of inner-ring creep in rolling bearings," *PhD Thesis*, KTH Royal Institute of Technology, Stockholm, Sweden, 2024.

[13] S. Murata and T. Onizuka, "Mechanism of creep in rolling bearings under transition fits," *NTN Technical Review*, no. 62, pp. 45–52, 1994.
[14] M. Schiemann and G. Poll, "Creep and fretting in interference fits of rolling bearings," *Wälzlagertechnik*, vol. 57, pp. 112–121, 2018.
[15] T. Niwa, "Traveling-wave-induced creep in bearing rings," *Journal of Tribology*, vol. 119, pp. 345–351, 1997.
[16] L. Zhou, X. Chen, and Y. Wang, "Micro-sliding and wear modelling in bearing ring interfaces," *Wear*, vol. 540, p. 204123, 2025.

DEPARTMENT OF MECHANICS AND MARITIME SCIENCES
CHALMERS UNIVERSITY OF TECHNOLOGY
Gothenburg, Sweden 2026
www.chalmers.se

CHALMERS
UNIVERSITY OF TECHNOLOGY